

A cloud detection algorithm-generating method for remote sensing data at visible to short-wave infrared wavelengths

Lin Sun ^{a,*}, Xuetong Mi ^{a,*}, Jing Wei ^a, Jian Wang ^b, Xinpeng Tian ^a, Huiyong Yu ^a, Ping Gan ^a

^a Geomatics College, Shandong University of Science and Technology, Qingdao, Shandong 266590, China

^b School of Geography, Beijing Normal University, Beijing 100875, China



ARTICLE INFO

Article history:

Received 19 March 2016

Received in revised form 28 September 2016

Accepted 14 December 2016

Available online 31 December 2016

Keywords:

Hyperspectral sensor

Multispectral sensors

Pixel dataset

Data simulation

Cloud detection

Cloud possibility

ABSTRACT

To realize highly precise and automatic cloud detection from multi-sensors, this paper proposes a cloud detection algorithm-generating (CDAG) method for remote sensing data from visible to short-wave infrared (SWIR) bands. Hyperspectral remote sensing data with high spatial resolution were collected and used as a pixel dataset of cloudy and clear skies. In this paper, multi-temporal AVIRIS (Airborne Visible/Infrared Imaging Spectrometer) data with 224 bands at visible to SWIR wavelengths and a 20 m spatial resolution were used for the dataset. Based on the pixel dataset, pixels of different types of clouds and land cover were distinguished artificially and used for the simulation of multispectral sensors. Cloud detection algorithms for the multispectral remote sensing sensors were then generated based on the spectral differences between the cloudy and clear-sky pixels distinguished previously. The possibility of assigning a pixel as cloudy was calculated based on the reliability of each method. Landsat 8 OLI (Operational Land Imager), MODIS (Moderate Resolution Imaging Spectroradiometer) Terra and Suomi NPP VIIRS (Visible/Infrared Imaging Radiometer) were used for the cloud detection test with the CDAG method, and the results from each sensor were compared with the corresponding artificial results, demonstrating an accurate detection rate of more than 85%.

© 2016 The Authors. Published by Elsevier B.V. on behalf of International Society for Photogrammetry and Remote Sensing, Inc. (ISPRS). This is an open access article under the CC BY-NC-ND license (<http://creativecommons.org/licenses/by-nc-nd/4.0/>).

1. Introduction

Covering more than 50% of the global surface, clouds play an important role in the radiative balance of the planet because of their absorption and scattering of solar and infrared radiation (Harshvardhan et al., 1989; King et al., 2013). Clouds influence the energy transfer between the sun and earth's surface by blocking radiation between them, causing the information in a cloud-covered region lost or blurred and reducing the data utilization rate (Carslaw et al., 2002; Goodwin et al., 2013; Hagolle et al., 2010; Yang et al., 2012; Sun et al., 2016). Cloud cover greatly affects the accuracy and reliability of parameter inversion, blocking the combination of different detected images and the quantitative inversion of detailed surface parameters (Kazantzidis et al., 2011, 2012; Li et al., 2011; Sun et al., 2016). It is important to acquire cloudless images automatically because of the large amount required for multi-temporal and large-scale studies. However, this acquisition is difficult due to climatic factors and a large observa-

tion range (Greenhough et al., 2005; Li et al., 2016). To date, only some microwave sensors can eliminate cloud cover and obtain qualified images in the acquisition of geospatial information through remote sensing technology (Chang and Li, 2005; Yang et al., 2013). Thus, the elimination of cloud cover regions by an efficient detection method is an urgent priority in remote sensing data processing (Nakajima et al., 2011; Sun et al., 2010).

A variety of cloud detection methods have been developed over the years, of which the threshold, radiative transfer and statistical methods are the most notable. The threshold cloud detection method has been widely applied because of its simple algorithm, fast operation and high precision of detection and is the most widely used cloud detection method (Hagolle et al., 2010; Jedlovec et al., 2008; Zhu et al., 2015). The most representative methods include ISCCP (International Satellite Cloud Climatology Project), CLAVR (Clouds from the Advanced Very High Resolution Radiometer (AVHRR), NOAA) and APOLLO (AVHRR Processing scheme Over cLOUDs, Land and Ocean) (Kriebel et al., 2003; Murino et al., 2014).

The ISCCP algorithm described by Rossow et al. (1985), Rossow and Schiffer (1991), Rossow and Garder (1993) assumes that the observed visible and infrared radiances are caused by only two

* Corresponding authors.

E-mail addresses: sunlin6@126.com (L. Sun), mixuetong@yeah.net (X. Mi).

types of conditions, cloudy and clear, and that the ranges of radiances and the variability associated with these two conditions do not overlap (Rossow and Garder, 1993). Comparing the observed pixel values with those of clear sky through a visible band of $0.6\text{ }\mu\text{m}$ and an infrared window of $11\text{ }\mu\text{m}$, a cloud pixel can be identified if at least one radiance value is distinct from the inferred clear value by an amount larger than the uncertainty in the clear threshold value. Uncertainty can be caused both by measurement errors and natural variability. This algorithm was constructed to be cloud-conservative, minimizing false cloud detections but missing clouds that resemble clear conditions (Zhu et al., 2015; Sun et al., 2016).

The NOAA CLAVR algorithm (Stowe et al., 1991), adopting a pixel matrix of 2×2 as the identification unit, can be used for global cloud detection. A cloud pixel is identified when all four pixels in the 2×2 pixel matrix pass the cloud detection test; otherwise, clear sky is identified. When only 1–3 pixels pass the test, the pixel matrix is mixed. A pixel matrix can be identified as clear sky when the pixels in a cloud or mixed matrix meet the conditions for ice/snow, oceanic specular reflection or a bright desert background. The algorithm is divided into four classes according to the underlying surface properties and observation time: ocean and land during the day and night, respectively (Greenhough et al., 2005; Kriebel et al., 2003; Lin et al., 2015).

The APOLLO algorithm described by Saunders and Kriebel (1988), Kriebel et al. (1989) and Gesell (1989) uses the detection data from the five full-resolution AVHRR channels to set a threshold in each channel according to the object characteristics to identify cloudy pixels. Based on the data, a pixel is identified as a cloud pixel when the threshold set by the reflectance is higher or the threshold set by temperature is lower. A pixel can be identified as clear sky if the reflectance ratio of channels 2 and 1 is between 0.7 and 1.1, the temperature difference between channels 4 and 5 is above a set threshold, and the spatial uniformity over the ocean is greater than a set threshold (Saunders and Kriebel, 1988); otherwise, the pixel is identified as being polluted by clouds. Completely covered cloudy pixels can be distinguished from partially covered pixels if they are tested with different thresholds (Kriebel et al., 2003; Sun et al., 2016).

In addition, other methods that are also widely used for cloud detection from satellite data. Zhang et al. developed a haze optimized transformation (HOT) algorithm to detect hazy/cloud spatial distributions in Landsat images, and this transformation was designed to minimize terrestrial surface effects (Zhang et al., 2002; Zhang and Guindon, 2003). A scene-average Automated Cloud Cover Assessment (ACCA) algorithm has been used for Landsat-7 ETM+ data since its launch by NASA in 1999; by applying a number of spectral filters, and the ACCA algorithm can well estimate the overall percentage of clouds in each Landsat scene (Irish et al., 2006). Hégarat-Mascle and André (2009) proposed an automatic detection algorithm for cloud and cloud shadow on visible high resolution optical images based on the use of Markov Random Field formalism on graphs and performed well on the experiments with fast convergence and low false alarm rates. Li et al. (2012) developed a new variational gradient-based fusion method for cloud detection with visible and short-wave infrared (SWIR) bands that enables spatial enhancement and dehazing of visible imagery. A spatial-temporal reflectance fusion method was also proposed for cloud detection by using the difference between the spatial and temporal information. Sedano et al. (2011) presented a new cloud detection method for high resolution remote sensing data based on pixel-based seed identification and object-based region growing. Evaluation results showed that it can get a high detection accuracy for clouds of different types over various land surfaces. Lin et al. (2015) introduced a new method for radiometric normalization and cloud detection of optical satellite images based on the

major axis of a scatterplot and the invariant pixels which can be determined by the proposed weighted PCA technology. Evaluation results indicated that it can perform well for multi-temporal images containing various landscapes. Sun et al. (2016) proposed a universal dynamic threshold cloud detection algorithm (UDTCDA) supported by a priori surface reflectance database and was applied to MODIS and Landsat 8 images for cloud test. Evaluation results showed that it can reduce the effects of mixed pixels and complex surface structures and obtain a high precision in cloud detection.

Clouds are generally characterized by a higher reflectance and lower temperature than the underlying earth surface. As such, simple visible and infrared window threshold approaches perform considerably well in cloud detection (Ackerman et al., 2010). In the threshold method, the determination of the threshold is a key factor that affects the classification accuracy. Traditional cloud detection thresholds are determined by the surface reflectance difference between the underlying surfaces and clouds, whereas the detection data are the apparent reflectance; however, the influence of the atmosphere in the radiative transfer process makes the surface reflectance different from the apparent reflectance. The difference in reflectivity and point-to-pixel expansion make the threshold unable to be effectively determined and affect the detection precision. In addition, we must study different cloud detection algorithms for different sensor data, which not only takes great effort but also reduces the application scope of the data, which is not conducive to future work. The automatic detection of clouds is not a simple task. A changing solar elevation angle and instrument viewing angles, limited spectral channels, instrument noise, and varying surface properties often limit the success of traditional cloud detection schemes when applied over a large area (Jedlovec et al., 2008). With the development and progress of science and technology, the realization of automated cloud detection has a wide range of applications and remote sensing requirements.

AVIRIS (Airborne Visible/Infrared Imaging Spectrometer) has measured spectral images for scientific research and applications every year since 1987 and was the first imaging spectrometer to measure the reflected solar spectrum from 400 nm to 2500 nm. AVIRIS measures the upwelling radiance through 224 contiguous spectral channels at 10 nm intervals across the spectrum. In the 400–2500 nm spectral range, molecules and particles from terrestrial, aquatic and atmospheric environments interact with solar energy through absorption, reflection, and scattering processes; therefore, this wavelength range is most commonly used for cloud detection (Green et al., 1998). AVIRIS has characteristics of high spatial resolution, spectral resolution and calibration accuracy. The spectral, radiometric, and spatial calibration of AVIRIS was determined in the laboratory and monitored inflight each year. More than 4 TB of AVIRIS data have been acquired since the initial flights that covered most parts of North America (Fig. 1), including vegetation, towns, lakes, bare soil, snow, glaciers and other land surface types (Green et al., 1998; Van der Meer, 1994). AVIRIS is currently the major source of high-spectral-resolution images. Fig. 2 shows the apparent reflectance differences between clouds and typical surfaces within the spectral range of 400–2500 nm of AVIRIS data.

Aiming at the above mentioned problems, this paper puts forward a cloud detection algorithm generating (CDAG) method for remote sensing data obtained at visible to SWIR wavelengths based on hyperspectral and high-spatial-resolution remote sensing data from AVIRIS. Most cloud detection algorithms judge the existence of clouds based on the results obtained from many cloud detection tests, using multispectral data acquired by sensors. In fact, an imager that has more bands can be expected to detect clouds efficiently and accurately (Nakajima et al., 2011). The CDAG algorithms make full use of every band in the visible to SWIR

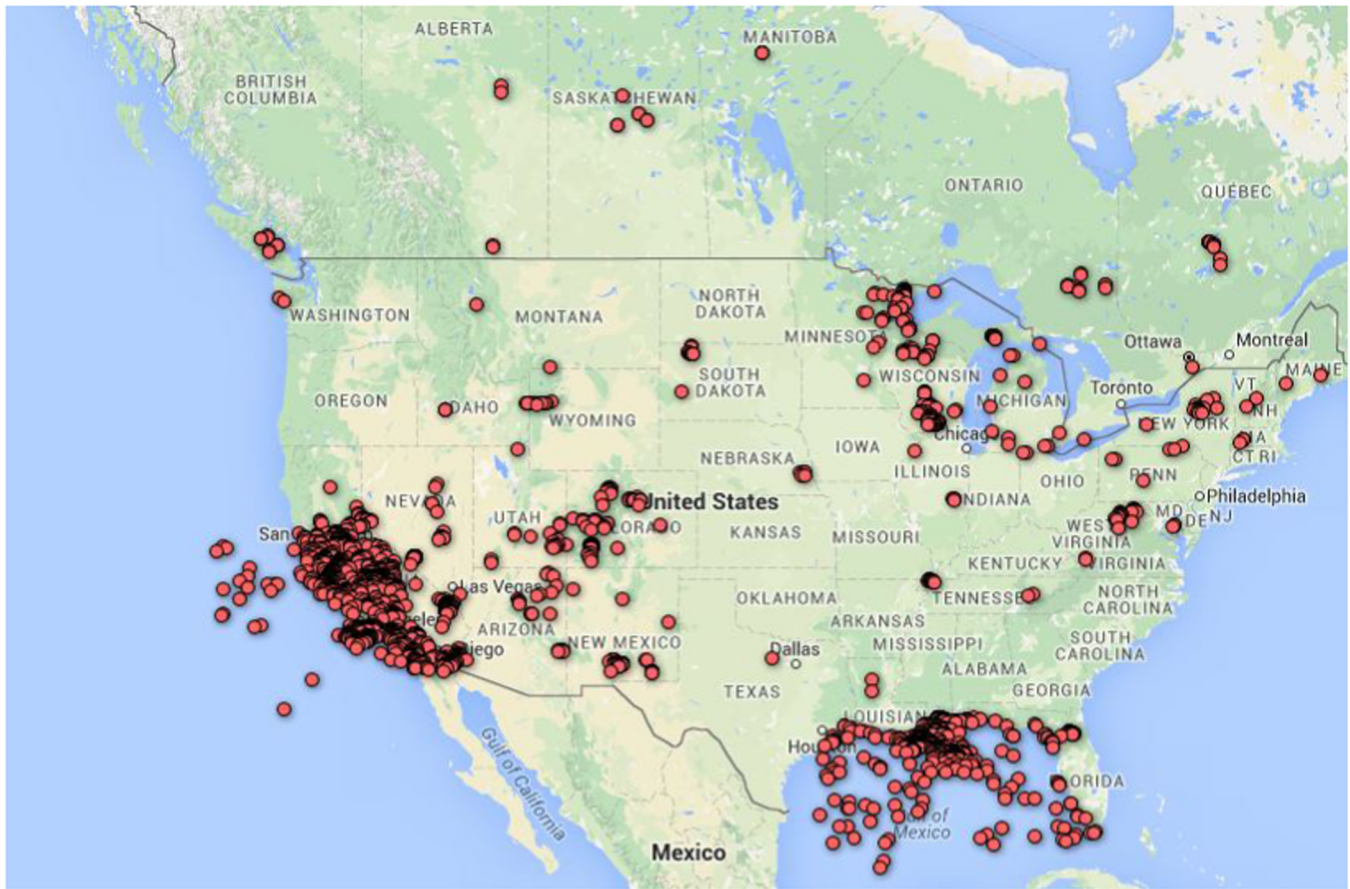


Fig. 1. AVIRIS data coverage area (from <http://aviris.jpl.nasa.gov/>).

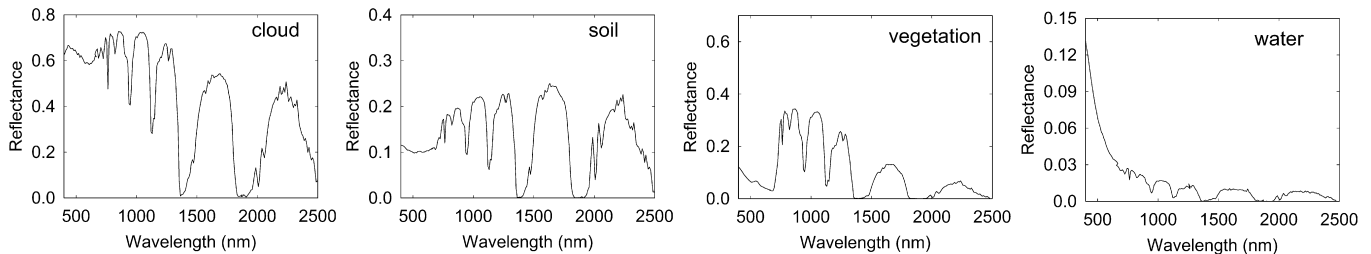


Fig. 2. Reflection spectra of clouds and typical surfaces from AVIRIS for clouds, soil, vegetables, and water, respectively.

wavelengths, and apply these bands to one or more spectral bands/or derived metrics.

The algorithms mainly carry out the following functions: pixel dataset establishment, data simulation, band operation, statistical analysis and weighted synthesis. The factors influencing cloud recognition not only involve the temporal and spatial distribution, but also the height, thickness and composition of the cloud. The pixel dataset containing various types of cloudy pixels and land cover is established in the preprocessing and mainly includes thin clouds, thick clouds, broken clouds, the edges of clouds, and clouds over water, vegetation, bare land, snow, glacier, etc. The pixels dataset from a hyperspectral sensor is transformed into a multispectral-version dataset using a band combination technique based on the spectral response function (SRF) of sensors and other parameters. The cloud detection algorithms for the multispectral remote sensing sensor are generated automatically in the next step based on the spectral difference between the clouds and underlying surfaces, and the synthetic cloud detection result is then

obtained according to the threshold and accuracy. In the experiments, the algorithm is applied to Landsat 8 OLI (Operational Land Imager) level 1T, Terra MODIS (Moderate Resolution Imaging Spectroradiometer) level 1B and Suomi NPP VIIRS (Visible/Infrared Imaging Radiometer) level 1 data, and accuracy statistics are presented. The CDAG algorithms are applicable to a variety of multi-sensor data and can eliminate or reduce the influence of clouds on image data.

2. Pixels dataset establishment

AVIRIS has been flown on two aircraft platforms: Q-bay of a NASA ER-2 aircraft, measuring images that are 11 km wide with a 20 m spatial resolution from an altitude of 20 km, and a Twin Otter turboprop, yielding a ground swath of approximately 2 km wide with a 4 m spatial resolution from an altitude of 4 km. Since the first spectral images were measured in 1987, AVIRIS data have

been widely used in the monitoring of the atmosphere, geological formations, soil, snow, ice and for satellite simulation, calibration, etc. (Baugh et al., 1998; Vane et al., 1993; Wei et al., 2015). The CDAG method was used to establish an apparent reflectance pixel dataset of cloudy and clear skies from 32 AVIRIS images acquired at different times and over different regions from 2007 to 2011. The 32 AVIRIS images were mainly acquired over South Carolina, Wisconsin, Nebraska, Michigan, Maine, Florida and other regions, covering the northeastern, southeastern and southwestern U.S. According to the associated statistics, the cloudy pixel dataset consisted of 398 blocks with a total of 425,283 pixels, and the clear-sky pixel dataset had 370 blocks with a total of 677,636 pixels. The cloudy and clear-sky pixels from AVIRIS were used as the ground truth for separating cloudy and clear-sky pixels by the cloud detection algorithm. Typical examples of the pixel dataset

are shown in **Tables 1** and **2**, in which the images are shown with wavelengths of 1681 nm, 841 nm, and 540 nm in red, green, and blue, respectively. The last column in the table compares the spectral curve of a pixel in the three images, and the red dot in the image is the selected pixel point.

To establish a more integrated cloud detection algorithm, a sufficient number of comprehensive cloud and surface types must be taken into account. To establish the cloud pixel dataset, we select thin clouds, thick clouds, broken clouds, and cloud edges, as well as the clouds over different types of underlying surfaces such as high vegetation coverage, bright surfaces, water, and mountains. **Table 1** lists typical examples of cloudy pixels and is divided into thick clouds, thin clouds and broken clouds. Based on the spectral curves, the reflectance of thick clouds is higher than those of thin clouds and broken clouds, and there are also differences in the

Table 1
Typical examples of cloudy pixels in the pixel dataset.

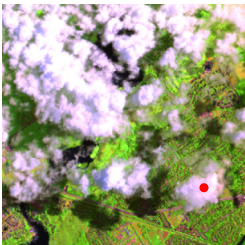
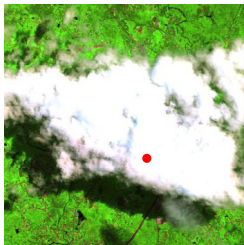
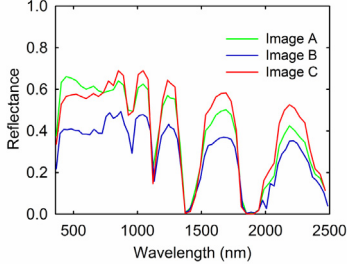
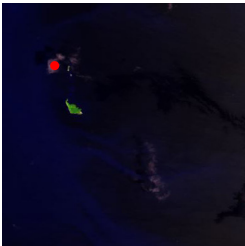
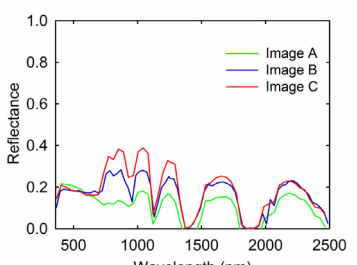
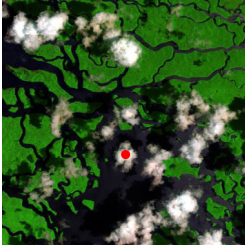
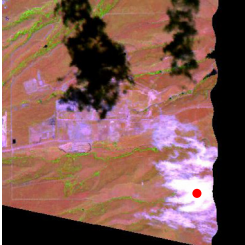
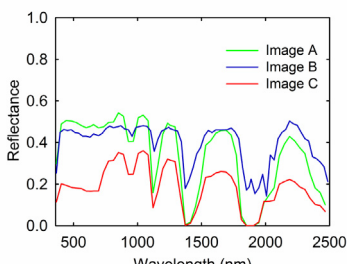
Class	Illustration	Spectral curve		
Thick cloud	 Image A: thick clouds above water Date: 20100523 Lon: 81°01'33"W Lat: 25°06'32"N	 Image B: thick clouds above town Date: 20110810 Lon: 89°23'16"W Lat: 43°09'18"N	 Image C: thick clouds above vegetation Date: 20090705 Lon: 71°04'53"W Lat: 43°02'06"N	
Thin cloud	 Image A: thin clouds above water Date: 20100523 Lon: 81°01'24"W Lat: 25°02'31"N	 Image B: thin clouds above building Date: 20110810 Lon: 89°20'42"W Lat: 43°08'20"N	 Image C: thin clouds above vegetation Date: 20090705 Lon: 71°30'17"W Lat: 42°52'11"N	
Broken cloud	 Image A: broken clouds above water Date: 20100523 Lon: 81°04'40"W Lat: 25°20'07"N	 Image B: broken clouds above rock Date: 20110807 Lon: 105°11'07"W Lat: 39°52'44"N	 Image C: broken clouds above vegetation Date: 20100826 Lon: 90°57'15"W Lat: 45°36'44"N	

Table 2

Typical examples of clear-sky pixels in the pixel dataset.

Class	Illustration	Spectral curve
Water		 The plot shows Reflectance on the Y-axis (0.0 to 1.0) versus Wavelength (nm) on the X-axis (500 to 2500). Three curves are shown: Ocean (green), River (blue), and Lake (red). All three curves show low reflectance across the entire wavelength range, with a slight increase in reflectance around 1000 nm.
Vegetation		 The plot shows Reflectance on the Y-axis (0.0 to 1.0) versus Wavelength (nm) on the X-axis (500 to 2500). Three curves are shown: FarmLand (green), Grass (blue), and Forest (red). The FarmLand curve has distinct peaks at approximately 700 nm and 1000 nm. The Grass curve has a broad peak around 700 nm. The Forest curve has a broad peak around 700 nm and a smaller peak around 1500 nm.
Artificial surface		 The plot shows Reflectance on the Y-axis (0.0 to 1.0) versus Wavelength (nm) on the X-axis (500 to 2500). Three curves are shown: Industrial land (green), Road (blue), and Town (red). The Industrial land curve has a sharp peak at approximately 1000 nm. The Road curve has a broad peak around 700 nm and a smaller peak around 1500 nm. The Town curve has a broad peak around 700 nm and a smaller peak around 1500 nm.
Other		 The plot shows Reflectance on the Y-axis (0.0 to 1.0) versus Wavelength (nm) on the X-axis (500 to 2500). Three curves are shown: Bare soil (green), Snow (blue), and Coastline (red). The Bare soil curve has a broad peak around 700 nm and a smaller peak around 1500 nm. The Snow curve has a very high reflectance peak at approximately 500 nm. The Coastline curve has a broad peak around 700 nm and a smaller peak around 1500 nm.

reflectivity of clouds over different underlying surfaces. The reflectance of thin clouds is lowest and is most affected by the underlying surface. In thin clouds, the reflectance above water is generally lower than the other two curves, especially in the near-infrared (NIR) spectral range.

Underlying surface characteristics change over time, especially in vegetation areas. To avoid temporal inconsistencies, the clear-sky pixel dataset is established on the basis of multi-temporal images. The clear-sky pixel dataset contains a variety of terrains, including mountains, plains, and oceans, and also includes

different land use types, such as woodlands, grasslands, paddy fields, dry fields, salt flats, urban areas, industrial land, bare soil, reservoirs, lakes, canals, and tidelands. Table 2 lists typical examples of clear-sky pixels which are divided into the following four categories according to the type of surface: water, vegetation, artificial surface and others. Water includes oceans, rivers and lakes; vegetation includes farmland, grass and forest; artificial surfaces include industrial lands, roads and towns; other typical surfaces include bare soil, snow and coastlines. Comparing the spectral curves of typical surfaces, the reflectance of water is the lowest, and there is a discrepancy between the three types of water because of the difference in surface properties, suspended solids content and nature. Snow, vegetation and artificial surfaces have higher reflectance and are prone to misjudgment.

Based on this comprehensive comparison, the reflectance of each band in areas with thick clouds is significantly higher than in cloudless regions, but the thin clouds and broken clouds are easily confused with the high-reflectance surfaces. Therefore, if a pixel dataset is not comprehensive, false positives for high-reflectance surfaces and false negatives for thin broken clouds can easily occur. Various surface types and a sufficient number of pixels are helpful in the study of cloud detection algorithms for use with different surface types and make the cloud detection algorithm more comprehensive.

3. Data simulation

Data simulation is a key step in the creation of a simulated multispectral pixel dataset for cloudy and clear skies at visible to SWIR wavelengths from a hyperspectral pixel dataset. Pixels of different types of clouds and land cover were artificially distinguished and used for the simulation of multispectral sensors. Compared with hyperspectral data, multispectral data has lower spectral resolution and a larger spectral coverage range, which could cover several spectral band subdivisions. A hyperspectral pixel dataset was simulated in order to obtain the apparent multispectral reflectance data of different types of clouds and land cover.

In this step, hyperspectral pixel datasets are combined into broader multispectral pixel datasets. Typically, data simulation is the process of combining several narrow hyperspectral bands to create one broader multispectral band, which is a redistribution of energy from the existing SRF in terms of energy transmission. In this process, the output energy of a multispectral band is related to its spectral response and the spectral energy corresponding to the hyperspectral data wavelength range. Each sensor used to obtain remote sensing images has a unique spectral characteristic that is embodied in its spectral band range and spectral responsivity. The spectral data for the remote sensing images are simulated using hyperspectral source data that covers the spectral range of the analog sensor to quantitatively simulate images from the analog sensor with known spectral properties. AVIRIS overcomes the limitations in band number, wavelength range and detailed information expression of traditional multispectral remote sensing and can be used as a data source to simulate remote sensing images. The spectral responses of the existing hyperspectral instrument AVIRIS are accurately approximated with Gaussian functions. This paper selected an AVIRIS pixel dataset as the data source for data simulation, which is the process of combining several hyperspectral bands to create one analog multispectral data input (Blonski et al., 2003; Green and Shimada, 1997; Zanoni et al., 2002).

Fig. 3 compares the spectral response curves between the multispectral sensor and AVIRIS. The first graph compares the Landsat 8 OLI Band 3 and AVIRIS spectral response curves in the wavelength range of 520–600 nm, the middle graph compares the VIIRS M8 and AVIRIS spectral response curves in the wavelength range of

1200–1260 nm, and the last graph compares the MODIS Band 7 and AVIRIS spectral response curves in the wavelength range of 2060–2180 nm.

Applying the band synthesis approach to the AVIRIS pixel dataset produces a multispectral sensor's pixel dataset whose apparent reflectance values are consistent with the apparent reflectance values of a coincident multispectral dataset when atmospheric radiative transfer effects are taken into account (Blonski et al., 2003; Green and Shimada, 1997). To obtain broadband multispectral data, we established the relationship between the hyperspectral data and multispectral data based on the predefined spectral response. The equations governing the data simulation process are shown here for completeness of the presentation. In this method, each band of the multispectral images is simulated by a weighted sum of the hyperspectral image bands. A total of 8 Landsat 8 OLI channels, 11 VIIRS channels and 20 MODIS channels are simulated from 400 nm to 2500 nm with 10 nm spectral resolution. In the current approach, calculation of the weights is based on finding the best approximation of a multispectral response through a linear combination of the hyperspectral responses.

$$R_i^{MSI}(\lambda_k) = \sum_{j=1}^{N_{HSI}} C_{ij} R_j^{HSI}(\lambda_k) \quad \text{for } k = 1, \dots, n, \quad i = 1, \dots, N_{MSI} \quad (1)$$

where N_{MSI} is the multispectral instrument band to be simulated and N_{HSI} is the AVIRIS band; the spectral response of the i th MSI band R_i^{MSI} is defined at n wavelengths λ^k ; the spectral response of the j^k HSI band R_j^{HSI} is also known for these wavelengths; the linear combination coefficients C_{ij} are derived by solving the least squares.

$$L_i^{MSI} = \frac{\sum_{j=1}^{N_{HSI}} C_{ij} \Delta_j L_j^{HSI}}{\sum_{j=1}^{N_{HSI}} C_{ij} \Delta_j} \quad \text{for } i = 1, \dots, N_{MSI} \quad (2)$$

where L_i^{MSI} is the pixel radiation value of the multispectral data (or the DN values or apparent values), L_j^{HSI} is the pixel AVIRIS radiation value, and Δ_j is the bandwidth of the AVIRIS data.

Through data simulation, a cloudy pixel is selected from the cloud pixel dataset, and the apparent multispectral reflectance values are obtained. The graph in Fig. 4 compares the apparent reflectance of cloudy pixels between AVIRIS and simulated multispectral data. From the apparent reflectance curve, the changes in reflectance of the Landsat 8 OLI, VIIRS and MODIS data are consistent with the change in the AVIRIS image.

An example of the image simulation is shown in Fig. 5 for the simulation of Landsat 8 OLI images from AVIRIS images, and histograms of the images are compared in Fig. 6 based on the spatial resolution difference. Similarities existed between the actual and simulated histograms, as expressed in both the shapes and positions of the peaks.

4. Cloud detection algorithm

4.1. Automatic generation method

The generation procedure of the cloud detection algorithm is shown in Fig. 7. The cloud detection algorithm generated in this paper is based on the difference in the reflection spectrum of clouds and underlying surfaces at visible to SWIR wavelengths. The reflectance properties of clouds are very similar to common features on the earth's surface, and the analysis of a particular band cannot detect the spectral difference at times. In this paper, all the bands and band combinations in the spectral range of 400–2500 nm are taken into account, and the multispectral pixel dataset is used as the truth in order to determine the spectral difference between cloudy and clear skies.

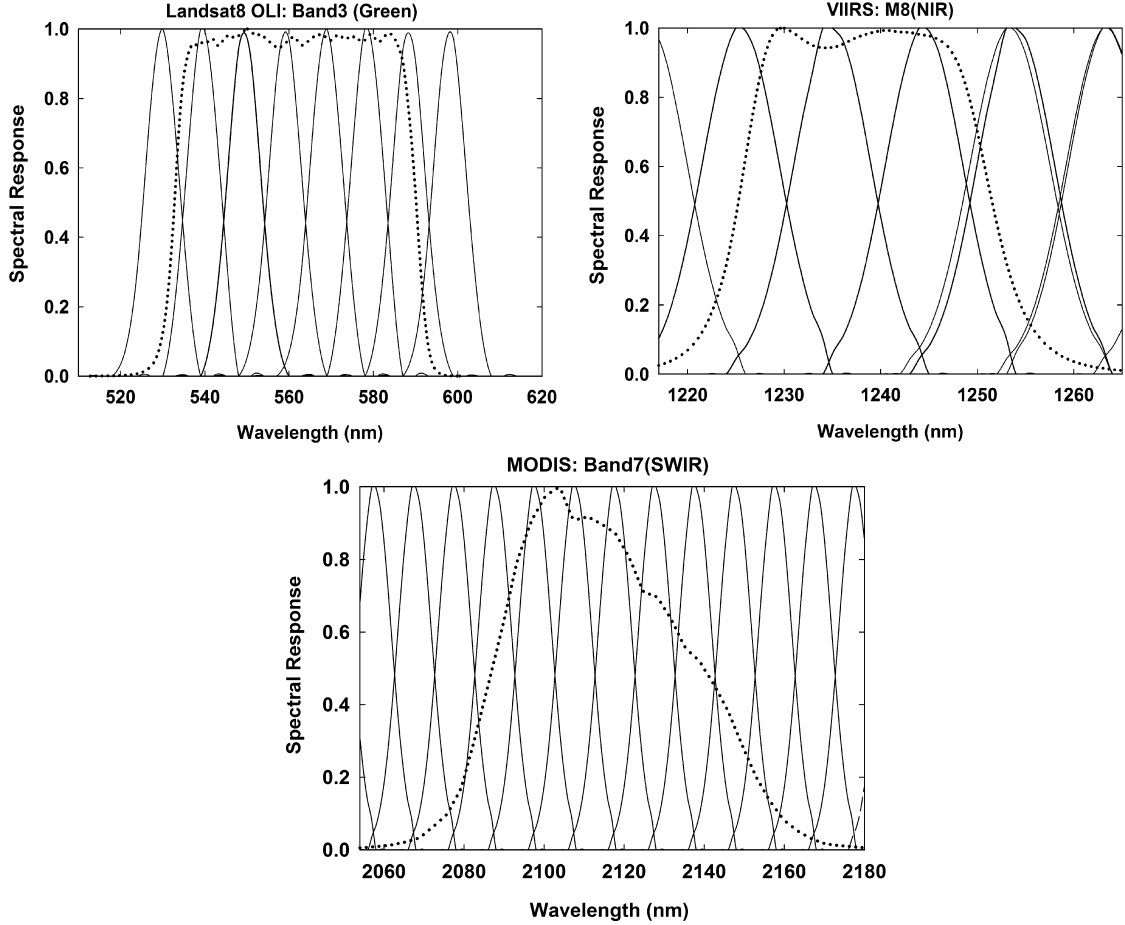


Fig. 3. SRF comparison of AVIRIS and multispectral data. In each graph, the hyperspectral AVIRIS components are shown as solid lines, and the spectral responses of the multispectral data are shown as dotted lines.

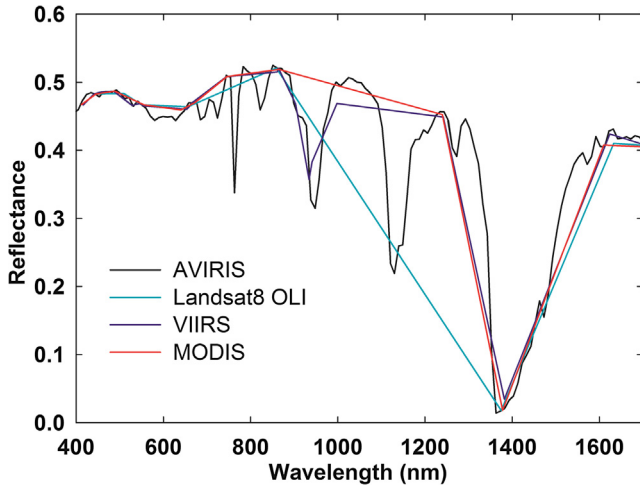


Fig. 4. Apparent reflectance contrast of a cloud pixel between the AVIRIS image and simulated multispectral image.

The algorithms generally used for cloud detection include single-band cloud detection, band-ratio cloud detection and the cloud detection index. To realize a more comprehensive cloud detection algorithm with fewer errors, this paper uses the band combinations that are normally used in the traditional cloud detection algorithms, considering minute spectral differences between

the underlying surface and clouds, and also adds two tests: the band-difference and band-ratio tests. These added tests can highlight cloud information and partially eliminate the influence of the solar elevation angle and satellite observation angle. Overall, the cloud detection algorithms used in this paper include the single-band test, multi-band test, band-ratio test, and band-difference test.

Because the time and region of an image affect the threshold values employed to detect clouds, these methods have some temporal and spatial limitations. Considering these limitations, this paper utilizes the spectral difference according to the sensor pixels dataset to be detected to determine a self-adaptive threshold. Limited by the 3% surface error rate, the threshold with the highest cloud pixel detection accuracy is taken as the best threshold. The surface error rate refers to the proportion of clear-sky pixels that are misjudged as cloudy pixels in the clear-sky pixel dataset. The threshold obtained in this way is more reasonable and applicable. Taking the single-band test as an example, all bands in the 400–2500 nm wavelength range of the sensor to be detected are involved in the single-band test. Firstly, we determine the cloud pixel reflectivity range of the band participated in band test, and the cloud pixel reflectance range is used as the threshold range. Secondly, the threshold value is changed in a step-wise manner over the threshold range, and the statistics of the accuracy of the cloudy pixels and the surface error rate, in which the step size of the threshold change is 0.01. The accuracy of cloudy pixels and the surface error rate changes with the threshold; when the accuracy of cloudy pixels reaches the highest value and is hardly

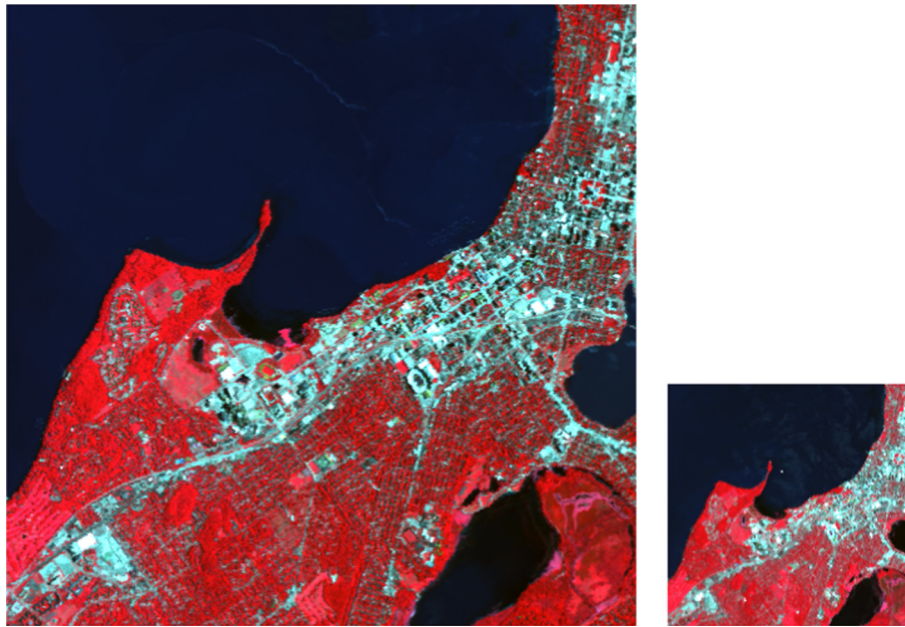


Fig. 5. False color Landsat 8 OLI image with 30 m spatial resolution of the Monona, Wisconsin, area at Path 24 and Row 30 acquired on July 15, 2015 (right), and the image synthesized from the AVIRIS data with 1 m spatial resolution acquired on August 10, 2011 (left). The two images are shown with bands 5, 4, and 3 composited. The area contains not only numerous roads but also vegetated spaces and a noticeable water surface, of which a dark signature is apparent in the histograms for the infrared bands.

affected by the threshold changes, the corresponding reflectance is the best threshold. As shown in Fig. 8, when the threshold reaches a value for which the accuracy changes little with increases in the threshold but the surface error rate increases significantly, then the value with the lowest misjudgment rate is taken as the best threshold. This automatic threshold determination method reduces the impact of subjectivity and makes the threshold more reasonable and reliable.

$$\text{Surface error rate} = \frac{\text{Clear-sky pixels misclassification of cloud pixels}}{\text{Total clear-sky pixels}} \quad (3)$$

$$\text{Accuracy of cloud pixels} = \frac{\text{The correct recognition of cloud pixels}}{\text{Total cloud pixels}} \quad (4)$$

The degree of coincidence of the tests generated in the previous step is assessed, and if the detection results of the two tests are the same, then one of them is deleted. The remaining algorithms are sorted according to the accuracy of the cloudy pixels. The detection results for a single pixel are largely dependent on the threshold. In many cloud detection algorithms, the results only include cloud and sky. For a cloud detection algorithm with $\rho_{0.66} > 0.21$, it is incorrect to consider the pixel as a cloud pixel because it is near pixel $\rho_{0.66} = 0.20$, which is clear sky. This affects the credibility of the data related to many factors, such as the equipment noise, ground spectral radiation characteristics, atmospheric humidity and aerosol scattering (Greenhough et al., 2005; Shi et al., 2008). CDAG presents the detection results according to the data credibility. In other words, considering any random value of [0, 1] as the credibility of the cloud detection results, the greater the value, the more credible the results. As shown in the following formula, if the observed value is greater than MAX, then we define the pixel as a completely cloudy pixel with a credibility of 1; if the observed value is less than MIN, then we define the pixel as a completely clear-sky pixel with a credibility of 0; if values are between MIN and MAX, then the credibility is between 0 and 1 and determined

by the distance from the pixel value to the threshold. The individual confidence flag indicates the confidence level for each single pixel test result.

$$S(x, \alpha, \beta, \gamma) = \begin{cases} 0 & (x \leqslant \text{MIN}) \\ (T - x)/(T - \text{MIN}) & (\text{MIN} \leqslant x \leqslant T) \\ (x - T)/(MAX - T) & (T \leqslant x \leqslant \text{MAX}) \\ 1 & (x \geqslant \text{MAX}) \end{cases} \quad (5)$$

4.2. Generation algorithms

To verify the cloud detection algorithm generation technology proposed in this paper, we chose the three most widely used multispectral data for validation: Landsat 8 OLI level 1T, Suomi NPP VIIRS level 1 and Terra MODIS level 1B.

4.2.1. Landsat 8 OLI cloud detection algorithms

Landsat 8 carries two sensors, OLI and TIRS (Thermal Infrared Sensor), which obtain over 500 image scenes per day. The OLI spectral bands remain broadly comparable to the Landsat 7 Enhanced Thematic Mapper plus (ETM+) bands (Sun et al., 2015). Compared to the ETM+, the OLI has two additional reflective wavelength bands. A new shorter wavelength blue band (0.43–0.45 μm) is intended to improve the sensitivity to chlorophyll and other suspended materials in coastal areas and enhance atmospheric aerosol properties. Another new shortwave infrared band (1.36–1.39 μm) can be used for cirrus cloud detection due to its strong absorption by water vapor. Other OLI bands consist of spectral bands that are narrower in most cases than the corresponding ETM+ bands (Roy et al., 2014; Zhu et al., 2015). In particular, the OLI NIR band is closer in width to the MODIS NIR band, which avoids the 0.825 μm water vapor absorption feature that occurs in the ETM+ NIR band. This paper uses the bands in the visible to SWIR wavelengths for cloud detection by the OLI sensor (Gao et al., 1993). The DN (Digital Number) of Landsat 8 OLI data can be converted to TOA spectral reflectance using the reflectance rescaling coefficients provided

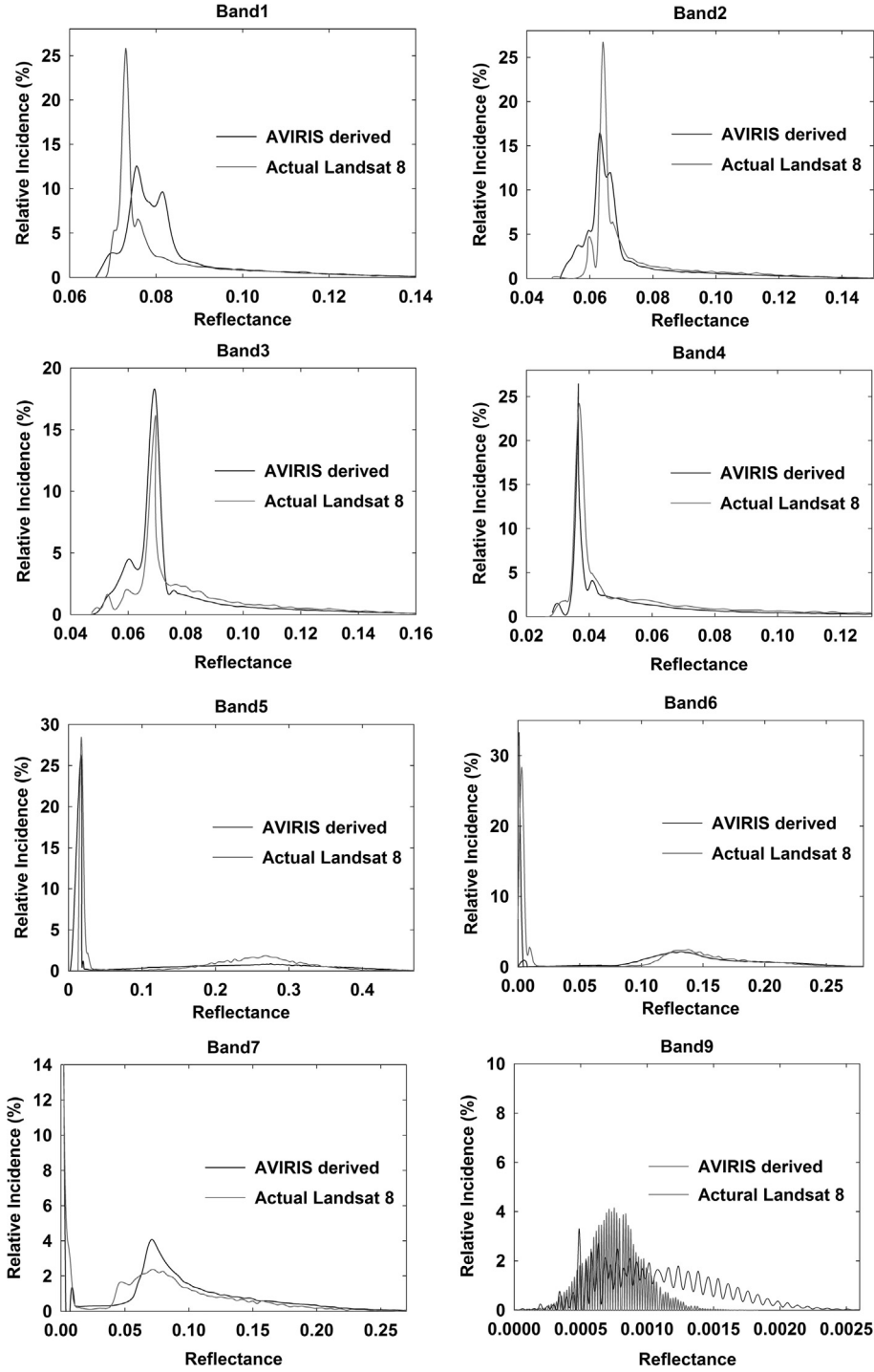


Fig. 6. Histograms of reflectance values for the actual Landsat 8 OLI and for the image simulated through spectral band synthesis from the AVIRIS data.

in the metadata (Sun et al., 2015). The band and bandwidths used as part of the cloud algorithm are listed in Table 3.

The cloud detection algorithm was generated automatically following the band test, coincidence degree determination and creation of the series of tests based on the multispectral pixel dataset. Table 4 gives the cloud detection algorithm for the Landsat 8 OLI data. The generated algorithm is comprehensive with an extensive range of coverage. Among these tests, the single-band test represents the case when the pixel value of the apparent reflectance is greater than the threshold value of the corresponding band, indicating that the pixels might be cloudy. The multi-band test lists the test bands used and the corresponding threshold val-

ues. When the apparent reflectance values of two bands are greater than the threshold value, the pixels are defined as cloudy. When the apparent reflectance ratios of two bands are between the minimum and maximum thresholds in cloud detection, in other words, when the ratio is greater than 1 and less than 1.08 in the VIIRS band-ratio test case study, the pixels might be cloudy. The band-difference test is similar to the band-ratio test.

4.2.2. Suomi NPP VIIRS cloud detection algorithms

The Suomi NPP satellite, launched on October 28, 2011, was the first satellite in the next-generation polar orbiting satellite system of the U.S. The NPP satellite, loaded with 5 earth observing systems

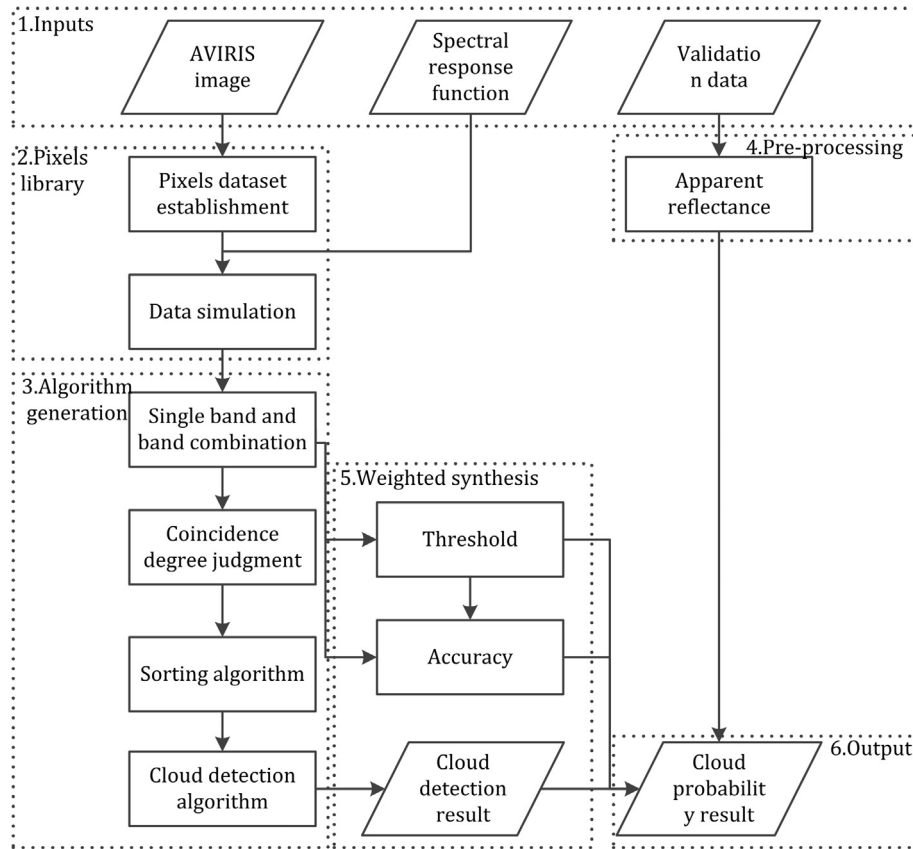


Fig. 7. Cloud detection procedural diagram.

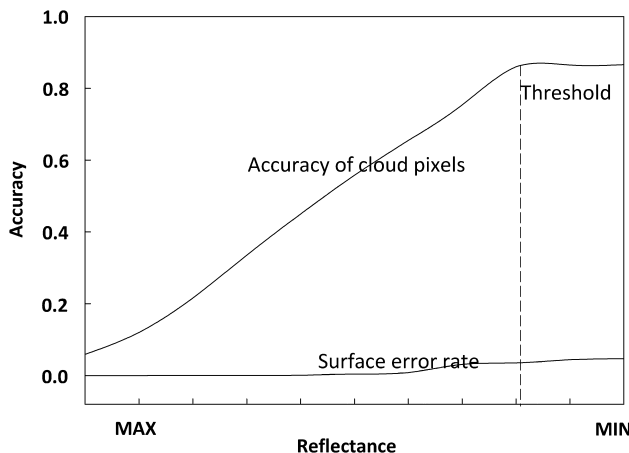


Fig. 8. Threshold determination.

including VIIRS, is also the next-generation earth observation satellite used to replace the Terra and Aqua satellites with extended use (Hillger et al., 2014). VIIRS is the result of the development and improvement of AVHRR and MODIS. The VIIRS sensor consists of 22 bands: 9 visible and NIR bands, 12 infrared and far-infrared bands, and a DNB (Day/Night Band). In addition, each pixel has a 12-bit quantization, and the total data rate reaches 10.5 Mbps (Hutchison et al., 2013). VIIRS is mainly used to monitor radiation changes of the land, atmosphere, ice and ocean in the visible and infrared bands, providing data for monitoring fires, vegetation, ocean color, ocean surface temperature and other surface changes (Kopp et al., 2014). This paper selected 11 bands from the VIIRS data with a wavelength range in the visible and SWIR region, and

the specific bands and bandwidths are listed in Table 3. Table 5 gives the cloud detection algorithm for the VIIRS data.

4.2.3. MODIS cloud detection algorithms

MODIS is an important sensor carried on the Terra and Aqua satellites, the data from which can be obtained for free. MODIS is a new optical remote sensing instrument that combines images and spectra. MODIS level 1B data consist of 36 discrete spectral bands covering a wide spectral range from 0.4 μm (visible) to 14.4 μm (thermal infrared) (Murino et al., 2014), and can provide information on land surface conditions; cloud properties; ocean color; phytoplankton; biogeography; chemistry; water vapor; aerosols; ozone; surface, atmospheric and cloud top temperatures; and cloud top height characteristics. In addition, MODIS level 1B data are temporally complementary, with at least 2 replicates obtained during the day and night, providing significant comprehensive analysis capabilities to earth science fields (Guo et al., 2013). A total of 20 bands in the visible to SWIR wavelengths were selected in this paper, and the specific bands and bandwidths are listed in Table 3. Table 6 gives the cloud detection algorithm for the MODIS data.

4.3. Weighted synthesis cloud results

Different underlying surfaces have different influences on cloud detection results, and different cloud detection algorithms have different detection contributions to the final results that mainly depend on the accuracy of the tests. If the credibility of the union is directly obtained, it will increase the errors of the cloud detection results, such that the misclassified pixels from every test will affect the final results. If the intersection of the detection results is obtained directly, cloud pixel information will be lost, which will

Table 3

Landsat 8 OLI, MODIS, and NPP VIIRS bands for cloud detection.

OLI bands (μm)	VIIRS bands (μm)	MODIS bands (μm)	MODIS bands (μm)
Band1 (0.433–0.453)	BandM1 ^a (0.412)	Band1 (0.620–0.670)	Band11 (0.526–0.536)
Band2 (0.450–0.515)	BandM2 ^a (0.445)	Band2 (0.841–0.876)	Band12 (0.546–0.556)
Band3 (0.525–0.600)	BandM3 ^a (0.488)	Band3 (0.459–0.479)	Band13 (0.662–0.672)
Band4 (0.630–0.680)	BandM4 ^a (0.555)	Band4 (0.545–0.565)	Band14 (0.673–0.683)
Band5 (0.845–0.885)	BandM5 ^a (0.672)	Band5 (1.230–1.250)	Band15 (0.743–0.753)
Band6 (1.560–1.660)	BandM6 ^a (0.746)	Band6 (1.628–1.652)	Band16 (0.862–0.877)
Band7 (2.100–2.300)	BandM7 ^a (0.865)	Band7 (2.105–2.155)	Band17 (0.890–0.920)
Band9 (1.360–1.390)	BandM8 (1.240)	Band8 (0.405–0.420)	Band18 (0.931–0.941)
	BandM9 (1.378)	Band9 (0.438–0.448)	Band19 (0.915–0.965)
	BandM10 (1.610)	Band10 (0.483–0.493)	
	BandM11 (2.250)		Band26 (1.360–1.390)

^a Represents a double-gain band.**Table 4**

Landsat 8 OLI cloud detection algorithm.

Single band	Multi band	Band ratio	Band difference
Band2 > 0.20	Band1 > 0.24&Band5 > 0.26	0.91 < Band6/Band7 < 1.83	0.21 < Band1– Band8 < 0.86
Band3 > 0.20	Band1 > 0.24&Band6 > 0.20		0.21 < Band2– Band8 < 0.89
Band4 > 0.21	Band2 > 0.16&Band5 > 0.26		0.23 < Band3– Band8 < 0.96
Band6 > 0.29	Band2 > 0.208&Band6 > 0.20		
Band7 > 0.25	Band3 > 0.12&Band5 > 0.32		
	Band4 > 0.14&Band5 > 0.35		
	Band5 > 0.408&Band6 > 0.30		
	Band5 > 0.408&Band7 > 0.14		

Table 5

NPP VIIRS cloud detection algorithm.

Single band	Multi band	Band ratio	Band difference
Band1 > 0.31	Band1 > 0.29&Band7 > 0.30	0.12 < Band6/Band4 < 0.48	0.29 < Band1– Band9 < 1.02
Band2 > 0.25	Band1 > 0.298&Band8 > 0.22	1.00 < Band7/Band5 < 1.15	
Band3 > 0.25	Band1 > 0.31&Band10 > 0.08		
Band4 > 0.25	Band1 > 0.29, Band11 > 0.12		
Band5 > 0.30	Band2 > 0.27&Band8 > 0.22		
Band7 > 0.52	Band2 > 0.27&Band10 > 0.14		
Band8 > 0.46	Band3 > 0.23&Band8 > 0.24		
	Band3 > 0.16&Band9 > 0.08		

misjudge the correct amount of cloudy pixels and thus increase the leakage assessment of the cloudy pixels. Considering the above factors, this paper generates a cloud probability map by weighting the different test results with the accuracy of the cloud detection algorithms. The probability level of the cloud probability map indicates the probability of determining cloudy pixels, with larger values representing a more credible presence of cloudy pixels. A probability of 1 indicates that the pixel is completely cloudy; a probability of 0 indicates that the pixel is completely clear sky. We could also limit the results to meet the needs of different users and obtain the

best cloud detection results. For example, the determination of ocean surface temperature is very sensitive to any type of cloud pollution, but some applications can tolerate pollution from thin cirrus clouds. Formula 6 calculates the probability of clouds, where F_i is the cloud detection result, Q_i is the accuracy corresponding to the cloud detection algorithms, and N is the total algorithm number of the multispectral data.

$$G = \frac{\sum_{i=1}^N Q_i F_i}{\sum_{i=1}^N Q_i} \quad (6)$$

Table 6

Terra MODIS cloud detection algorithm.

Single band	Multi band	Band ratio	Band difference
Band1 > 0.29	Band1 > 0.28&Band5 > 0.24	0.95 < Band2/Band1 < 1.15	0.19 < Band1– Band18 < 0.85
Band3 > 0.23	Band1 > 0.28&Band6 > 0.16		0.11 < Band1– Band19 < 0.45
Band8 > 0.29	Band2 > 0.34&Band10 > 0.20		0.22 < Band3– Band20 < 0.72
Band10 > 0.24	Band3 > 0.16&Band17 > 0.28		0.28 < Band9– Band20 < 0.95
Band11 > 0.24	Band5 > 0.248&Band10 > 0.30		0.23 < Band10– Band20 < 0.705
	Band6 > 0.168&Band10 > 0.30		
	Band6 > 0.22&Band17 > 0.28		
	Band7 > 0.08&Band8 > 0.28		
	Band8 > 0.25&Band17 > 0.27		
		

5. Experimental results and accuracy evaluation

5.1. Experimental results

This paper selects a plurality of Landsat 8 OLI, MODIS level 1B and NPP VIIRS images of different regions and at different times in 2010–2014 for validation, which includes not only thin, thick and broken clouds but also marine, land, sand, snow and other types of underlying surfaces. Validation of the CDAG is performed on many different scales because different types of errors are revealed with each approach. Selecting images at different times and of different underlying surfaces makes the verification results more comprehensive, accurate and reliable. Of the images selected, OLI has 26 scenes, MODIS has 35 scenes and VIIRS has 43 scenes.

5.1.1. Landsat 8 OLI experimental results

Fig. 9 displays the cloud detection results of two Landsat 8 OLI scenes. **Fig. 9A** shows the results from Inner Mongolia, China, over highly vegetated areas acquired on June 16, 2014, with a center longitude at 120°E and a center latitude at 50°N; **Fig. 9B** shows the results from Nagasaki, Japan, acquired on January 17, 2014, with a center longitude at 130°E and a center latitude at 33°N. The territories of these two Landsat 8 OLI scenes are complicated, including a variety of land cover types such as oceans, mountains, and towns. In each OLI scene, the upper left image shows an entire false color composited OLI image with bands 5, 4, and 3 as red, green and blue, respectively, and the upper right image shows the corresponding cloud detection result for the whole scene, with the white parts representing the cloudy pixels and the black parts representing the clear-sky pixels. The lighter areas the image correspond to more credible results. The lower left and lower right images are enlargements of the yellow boxes in the upper left and upper right images, and the size of this area is 25 × 25 km². A different degree of cloud cover can be observed in the two Landsat 8 OLI scenes by visually comparing the CDAG results with the

false color composites (**Fig. 9A and B**), which appears to work well in identifying clouds (white) with a cloud form that is complete and natural and clear sky (black). Thick clouds, as well as thin and broken cloud coverage, can be detected in the enlargements of the two Landsat 8 OLI scenes in the lower right corner and above in **Fig. 9A and B**.

To better observe the details and detection results, this paper selects a representative sub-image from the original false color image with underlying surfaces that include snow, soil, vegetation and water to display the results. In each scene of **Fig. 10**, the left side contains composite false color Landsat 8 images, and the right side contains the cloud detection results; brighter images correspond to more credible results. **Fig. 10A** is an image of the Malacca Strait region with thin and broken clouds covering the ocean and land areas. These detection results could identify thin and broken clouds over the ocean area without a misjudgment of ocean and land. Generally, it is easy to misjudge a bright surface area as cloudy pixels. In the urban area shown in **Fig. 10B**, high circus clouds cover the urban area in the composite false color image that are easily identified in the detection results with the corresponding overall outline and range. There are broken clouds in **Fig. 10C and D**, and the cloud detection results recognize broken clouds and a cloud edge region completely. There are thin clouds in **Fig. 10E and F**, and the contrast and false color composite images reveal that the detection results can identify most of the thin clouds. The algorithm can separate urban land from clouds, which could effectively remove thick clouds but miss part of the thin clouds in some regions. The above analysis of the cloud detection results demonstrates that the CDAG method described in this paper can yield better detection results over different underlying surfaces with different cloud detection algorithms and that clouds could be accurately and reliably identified at different times over different underlying surfaces.

To further evaluate the effectiveness of the proposed method in cloud detection, the cloud detection algorithm for Landsat 8 OLI

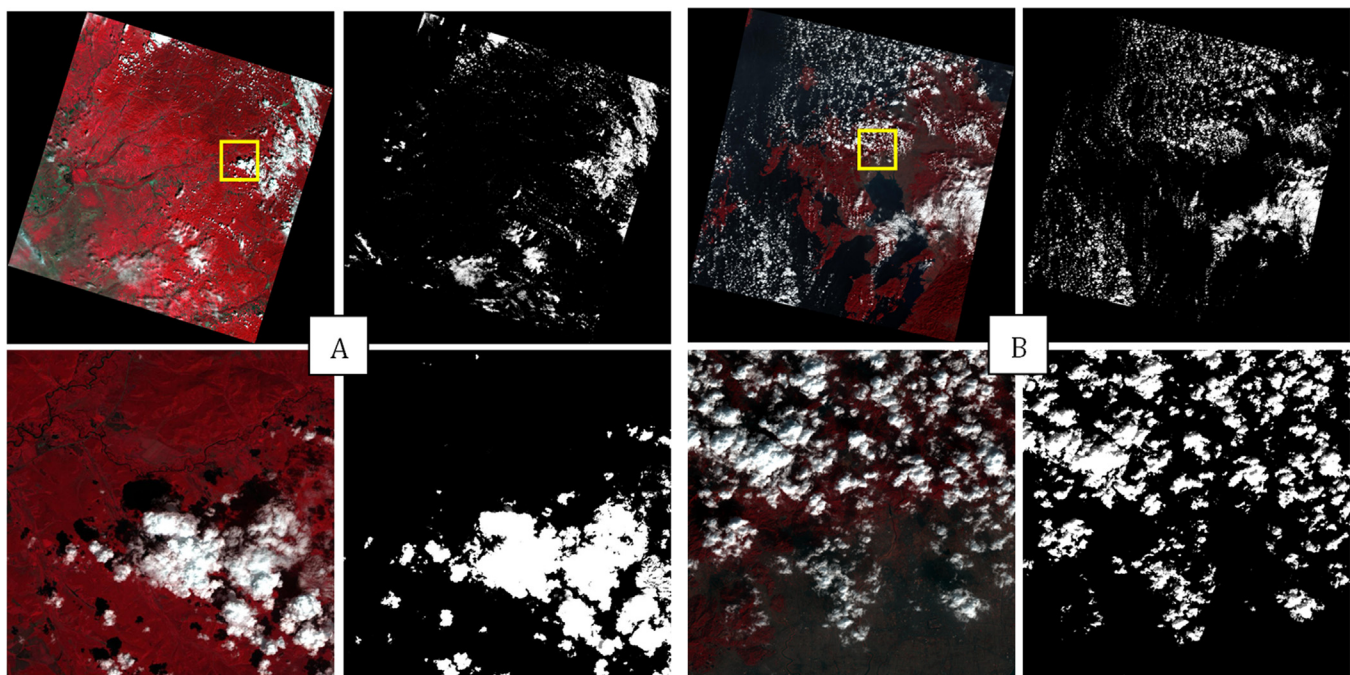


Fig. 9. Cloud detection results of two Landsat 8 OLI scenes. A: Results of Inner Mongolia, China, at Path 123 and Row 25 acquired on June 16, 2014. B: Results of Nagasaki, Japan, at Path 113 and Row 37 acquired on January 17, 2014. In each OLI scene, the (upper left) shows an entire false color composited OLI image, and the (upper right) shows the corresponding cloud detection result for the whole scene. Black pixels are clear sky. The (lower left) and (lower right) images are enlargements of the (upper left) and (upper right) images, with a size of 25 × 25 km². The false color composited image of two Landsat 8 OLI scenes is shown with bands 5, 4 and 3 as red, green and blue, respectively. (For interpretation of the references to color in this figure legend, the reader is referred to the web version of this article.)

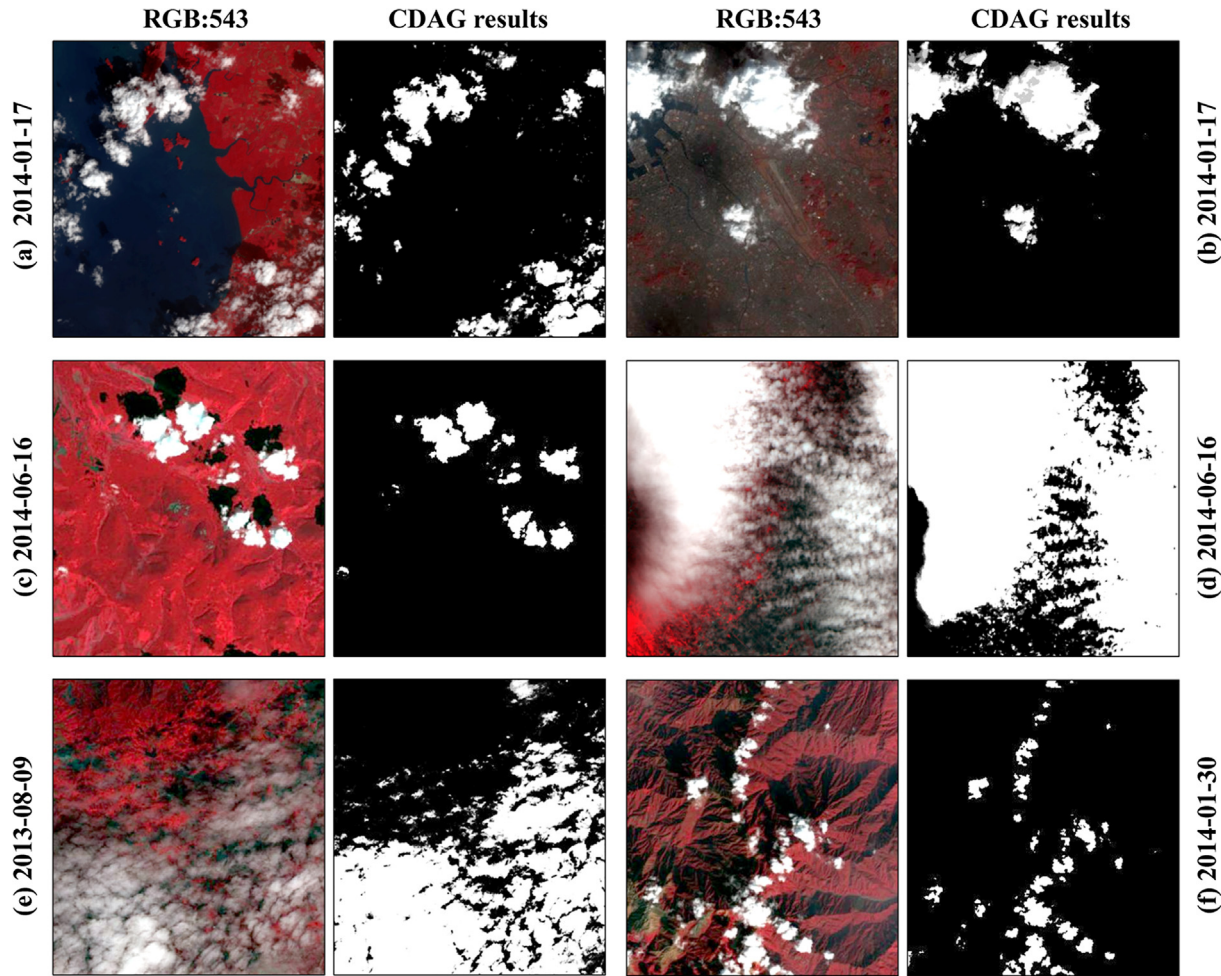


Fig. 10. Cloud detection results of Landsat 8 OLI scenes. A: Results of the Malacca Strait region at Path 129 and Row 54 acquired on January 17, 2014. B: Results of the Hakatawan region at Path 113 and Row 37 acquired on January 17, 2014. C: Results of Japan at Path 123 and Row 25 acquired on June 16, 2014. D: Results of Guilin, China, at Path 124 and Row 42 acquired on June 16, 2014. E: Results of Shandong Province, China, at Path 122 and Row 35 acquired on August 9, 2013. F: Results of Japan at Path 107 and Row 34 acquired on January 30, 2014. In each scene, the left shows a false color composited Landsat 8 image with bands 5, 4 and 3 as red, green and blue, respectively, and the right shows the detection results. Cloud detection results in black represent clear sky pixels, and white represents cloudy pixels. The brighter the image, the more credible the results. (For interpretation of the references to color in this figure legend, the reader is referred to the web version of this article.)

generated from this method was compared with a new version of Fmask (Function of mask). The Fmask algorithm was originally developed for masking clouds, cloud shadows, and snow for Landsats 4–7 and is now expanded to the Landsat 8 scenario by taking advantage of the cirrus band. Using an object-based cloud and cloud shadow matching algorithm, Fmask is capable of providing cloud, cloud shadow, and snow masks for each individual image. The cloud mask is computed from a probability mask and a scene-based threshold. Cloud shadows are calculated using a combination of previous methods (object matching and lapse rates) and a flood-fill transformation. The Fmask algorithm works well at high latitudes, accurately separating clouds from shadows or turbid water, and can also detect thin clouds and their shadows. This algorithm has been widely used and has been integrated into the Landsat surface reflectance Climate Data Record (CDR) provided by the Earth Resources Observation and Science (EROS) Center of the U.S. Geological Survey (USGS) (Maiersperger et al., 2013; Zhu and Woodcock, 2012, 2014; Zhu et al., 2015). To verify the cloud detection results produced by the CDAG algorithms, parts of the Landsat8 OLI cloud detection results were chosen to compare with the Fmask cloud detection results. To maintain the consistency of these two results, only cloud detection results from Fmask were used. A comparison of these results is shown in Fig. 11.

In each scene, the left shows the false color composite image with bands 5, 4 and 3; the middle shows are the cloud results of the CDAG algorithms; and right shows the Fmask results. Generally, the CDAG and Fmask algorithms accurately identify most of the cloudy pixels. However, the clouds identified by Fmask are slightly larger in extent than those identified in the CDAG results. The major reason for this difference is that Fmask uses a scene-based threshold and applies this same threshold to all pixels, which misclassified some clear pixels as clouds. Fig. 11A and E shows that the Fmask results overestimated the cloud region. As a result, very thin and small pieces of clouds are easily missed. Fig. 11B–F in the yellow box show that some thin clouds were misjudged as clear land pixels.

5.1.2. VIIRS experimental results

Multi-temporal VIIRS images were adapted to the CDAG algorithm, and the test results demonstrate that the CDAG algorithm can accurately identify clouds over different underlying surfaces in the VIIRS data, especially thin clouds. The detection results of each scan have the shape of a bow tie because the scan is further from the nadir. The striping at the edge of the image is due to the aggregation and deletion of overlapping pixels in order to reduce the “bow-tie effect” when imaging. Fig. 12 presents the

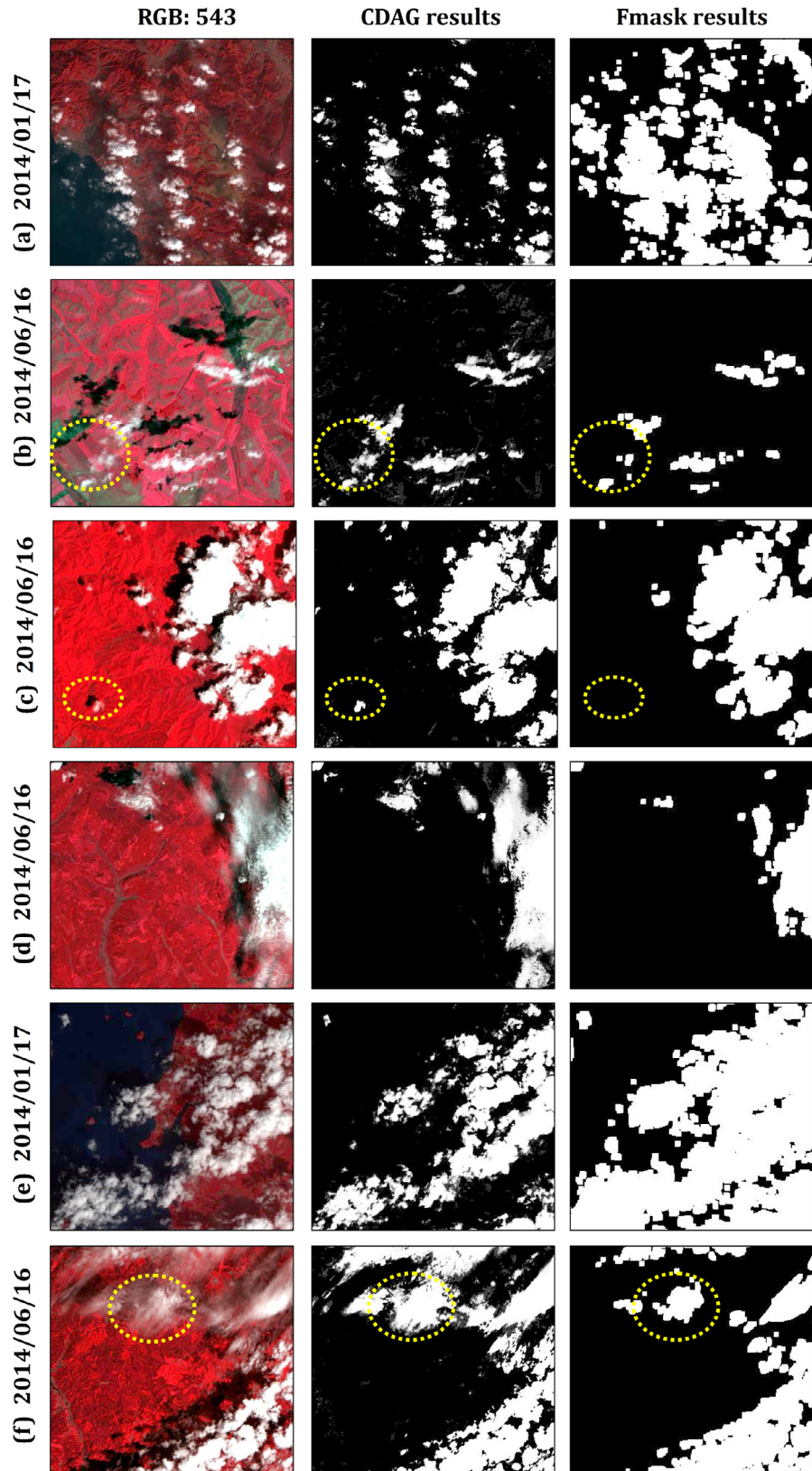


Fig. 11. Comparison of the CDAG and Fmask results for Landsat 8 OLI data. A: Results of the Hirado-shima region at Path 113 and Row 37 acquired on January 17, 2014. B: Results of the Hulun Buir region at Path 123 and Row 25 acquired on June 16, 2014. C: Results of the Gunma-ken region at Path 107 and Row 35 acquired on June 16, 2014. D: Results of the Hulun Buir region at Path 123 and Row 25 acquired on June 16, 2014. E: Results of the Krabi region at Path 123 and Row 25 acquired on January 17, 2014. F: Results of the Ibaraki-ken region at Path 107 and Row 35 acquired on June 16, 2014. In each scene, the left shows a false color composited Landsat 8 OLI image with bands 5, 4 and 3 as red, green and blue, respectively, in the middle of the CDAG results, and the right shows the Fmask result. (For interpretation of the references to color in this figure legend, the reader is referred to the web version of this article.)

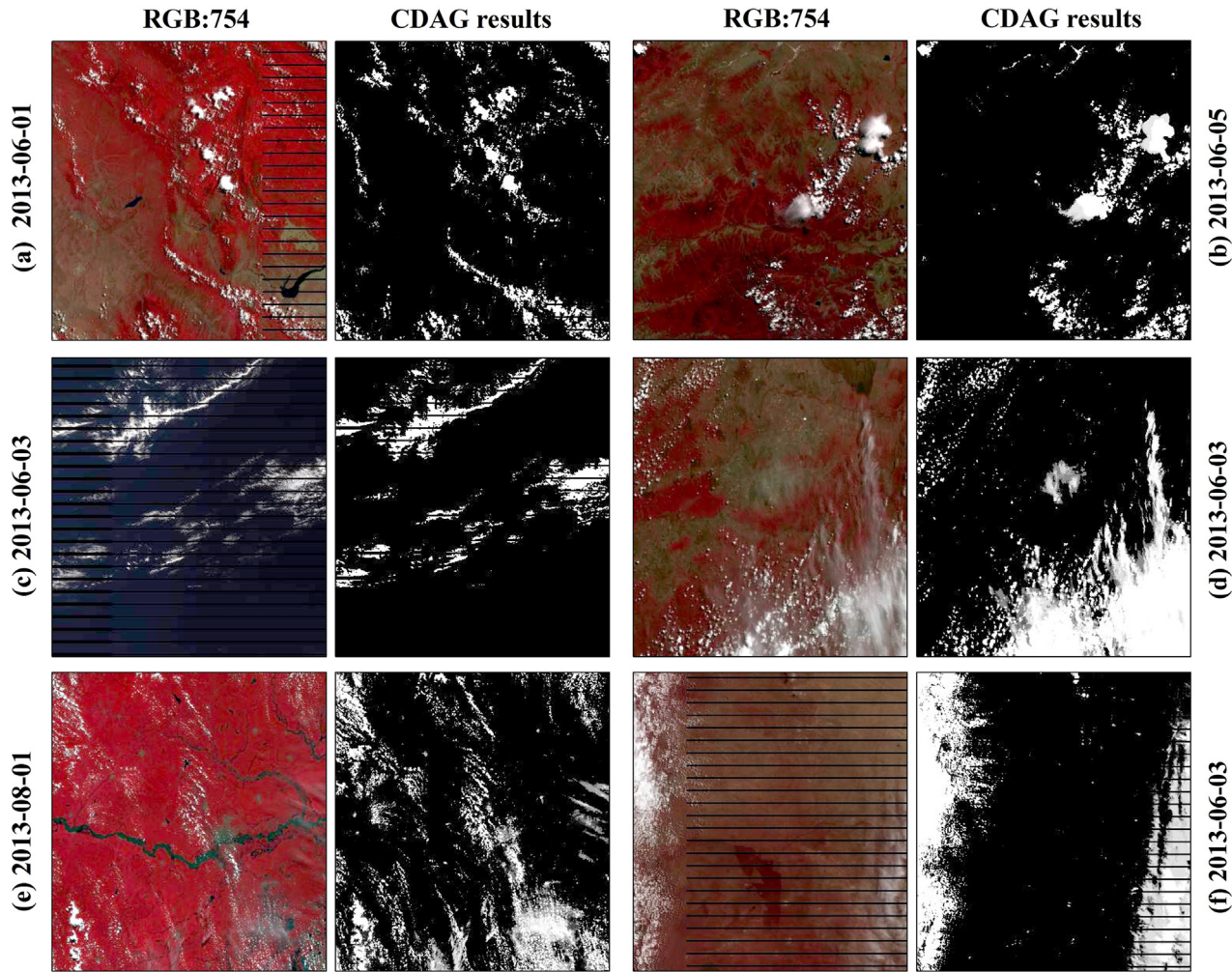


Fig. 12. Cloud detection results of NPP VIIRS scenes. A: Results of the VIIRS scene acquired on June 1, 2013. B: Results of the VIIRS scene acquired on June 5, 2013. C: Results of the VIIRS scene acquired on June 3, 2013. D: Results of the VIIRS scene acquired on June 3, 2013. E: Results of the VIIRS scene acquired on August 1, 2013. F: Results of the VIIRS scene acquired on June 3, 2013. In each scene, the left shows a false color composited VIIRS image with bands 7, 5 and 4 as red, green and blue, respectively, and the right shows the detection results. Cloud detection results in black represent clear sky pixels, and white represents cloudy pixels. The brighter the image, the more credible the results. (For interpretation of the references to color in this figure legend, the reader is referred to the web version of this article.)

cloud detection results of the VIIRS data. In Fig. 12A and B, all of the clouds are broken and well recognized, and the result is not affected by the underlying surface. There is a large region of thin clouds in the images of Fig. 12C–F that was easily identified. This algorithm can correctly identify thin clouds and their edges over areas of vegetation and water, and the results with the VIIRS data are well recognized overall.

5.1.3. MODIS experimental results

Fig. 13 displays the cloud detection results from the MODIS data, in which the false color image is composed from bands 2, 1 and 4. Based on this image, the algorithm can effectively identify the clouds over different underlying surfaces such as soil, water, vegetation and sandy land. The detection of thin clouds and cirrus clouds is greatly improved. There are a large number of thin clouds in the cloud edge region. These clouds have lower reflectance and are not easy to detect. The cloud detection algorithm proposed in this paper can effectively detect thin clouds based on the different characteristics of thin, cirrus and thick clouds and other underlying surfaces. In Fig. 13, the underlying surface of image E consists of the Gobi Desert and the desert in the Arabic region of image D, both of which have a typical tropical desert climate and are covered with thin clouds to different degrees in the image. Broken

clouds can also be detected over different underlying surfaces, as shown in images C and E.

MOD35 is a product of the MODIS data that detects objects based on the reflection of short-wave radiation by clouds and surfaces and of infrared radiation by itself. A description of this algorithm can be found in Ackerman et al. (1998) and Frey et al. (2008). MOD35 detects clouds from instruments that rely on a series of sequential tests of the radiances or their associated brightness temperatures. To verify the cloud detection results, parts of the MODIS cloud detection results are chosen to compare with the quasi-synchronous MODIS cloud detection products (MOD35). The comparison results are shown in Fig. 14. In the MOD35 cloud mask, only four credibility ratings are provided. Numerical values are assigned to each rating: white represents clouds with a credibility of greater than 0.99, red represents uncertain clear skies with a credibility between 0.95 and 0.99, blue represents probable clear skies with a credibility of 0.66–0.95, and black represents confident clear sky with a credibility of less than 0.66. Fig. 14A shows the region near Lake Baikal, and Fig. 14B shows the coastal area of the Bohai Sea; the upper right corner of both images distribute a certain amount of thin clouds and broken clouds. In the corresponding MOD35 image, the Lake Baikal lakeside is misjudged as uncertain clear, and some areas of the Bohai coast are misjudged

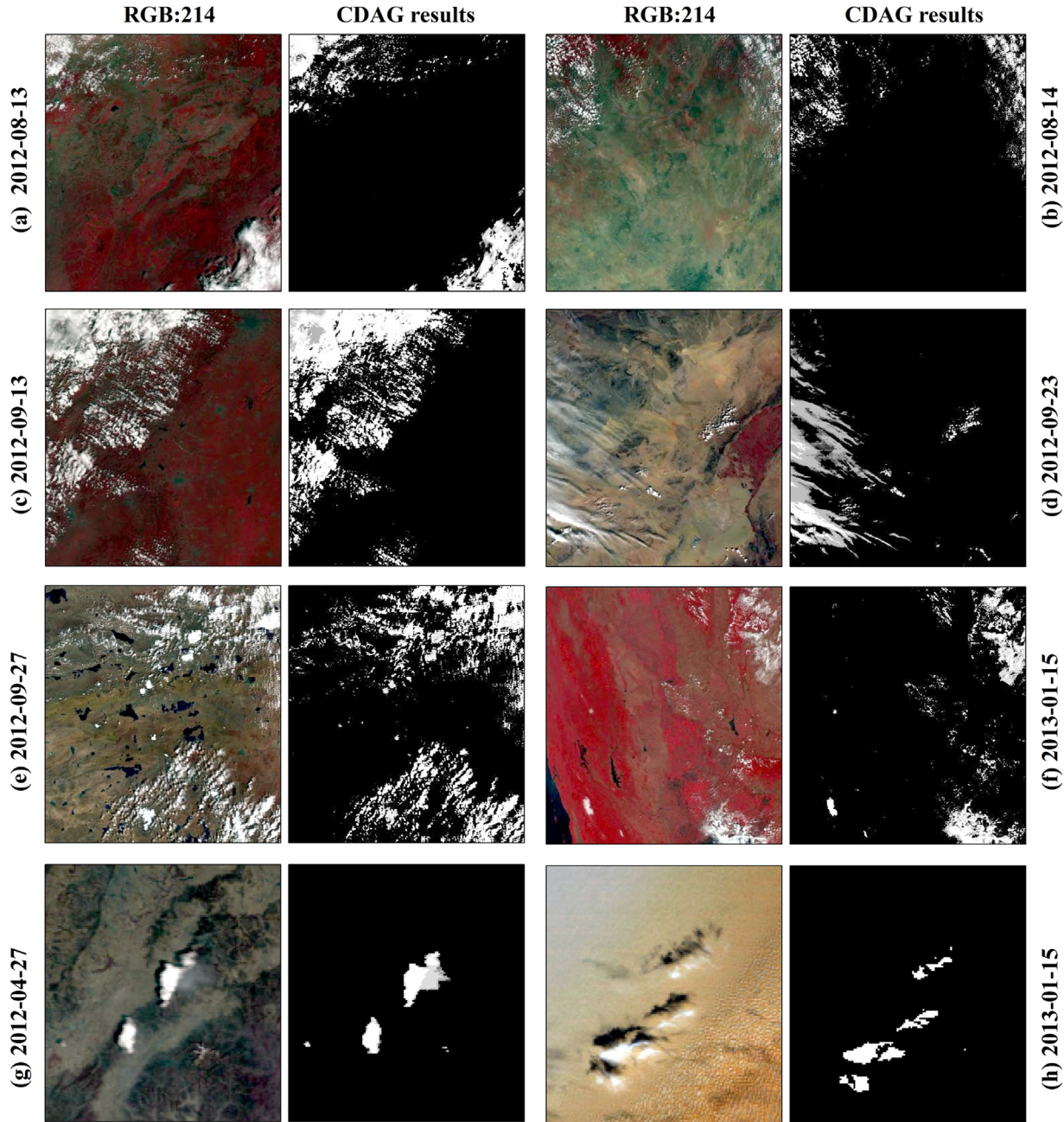


Fig. 13. Cloud detection results of MODIS level 1B scenes. A: Results of the Hohhot region, China, acquired at 0320 UTC time on August 13, 2012. B: Results of the Mongolia region acquired at 0400 UTC time on August 14, 2012. C: Results of the Baiyang Lake region, China, acquired at 0315 UTC time on September 13, 2012. D: Results of the Badain Jaran Desert region acquired at 0350 UTC time on September 23, 2012. E: Results of the Taklimakan Desert region acquired at 0505 UTC time on September 27, 2012. F: Results of the Andaman Sea region acquired at 0345 UTC time on January 15, 2013. G: Results of the Shanxi Province, China, acquired at 0335 UTC time on April 27, 2012. H: Results of the Arab region acquired at 0705 UTC time on January 15, 2013. In each scene, the left shows a false color composited MODIS image with bands 2, 1 and 4 as red, green and blue, respectively, and the right shows the detection results. Cloud detection results in black represent clear sky pixels, and white represents cloudy pixels. The brighter the image, the more credible the results. (For interpretation of the references to color in this figure legend, the reader is referred to the web version of this article.)

as cloudy, as shown in the yellow box. Fig. 14C displays result for Tibetan region in China; part of the area over water is misjudged as cloudy, and some broken clouds were missed in the MOD35 image, as shown in the yellow box. Based on the above comparison of the cloud detection results and MOD35 results, the CDAG algorithm proposed in this paper has less misjudgment over some water surfaces.

The visual interpretation and analysis of these three datasets demonstrates that the cloud detection algorithm in this paper is suitable for multi-sensor cloud detection and can achieve good results over different types of underlying surfaces. The detection of thin clouds and broken clouds has also been improved.

5.2. Accuracy evaluation

To evaluate the algorithm more comprehensively, qualitative analysis is performed on a large number of cloud detection results. The three types of data are vectorized manually, and the vectorization results are compared as reference images with the cloud detection results to calculate the accuracy of the cloudy and clear-sky pixels, the misjudgment ratio and the error ratio. Taking the vectorization images as reference data to compare with cloud detection results (Goodwin et al., 2013; Sun et al., 2016). Here, the following four indexes are selected for cloud detection assessment at the pixel level:

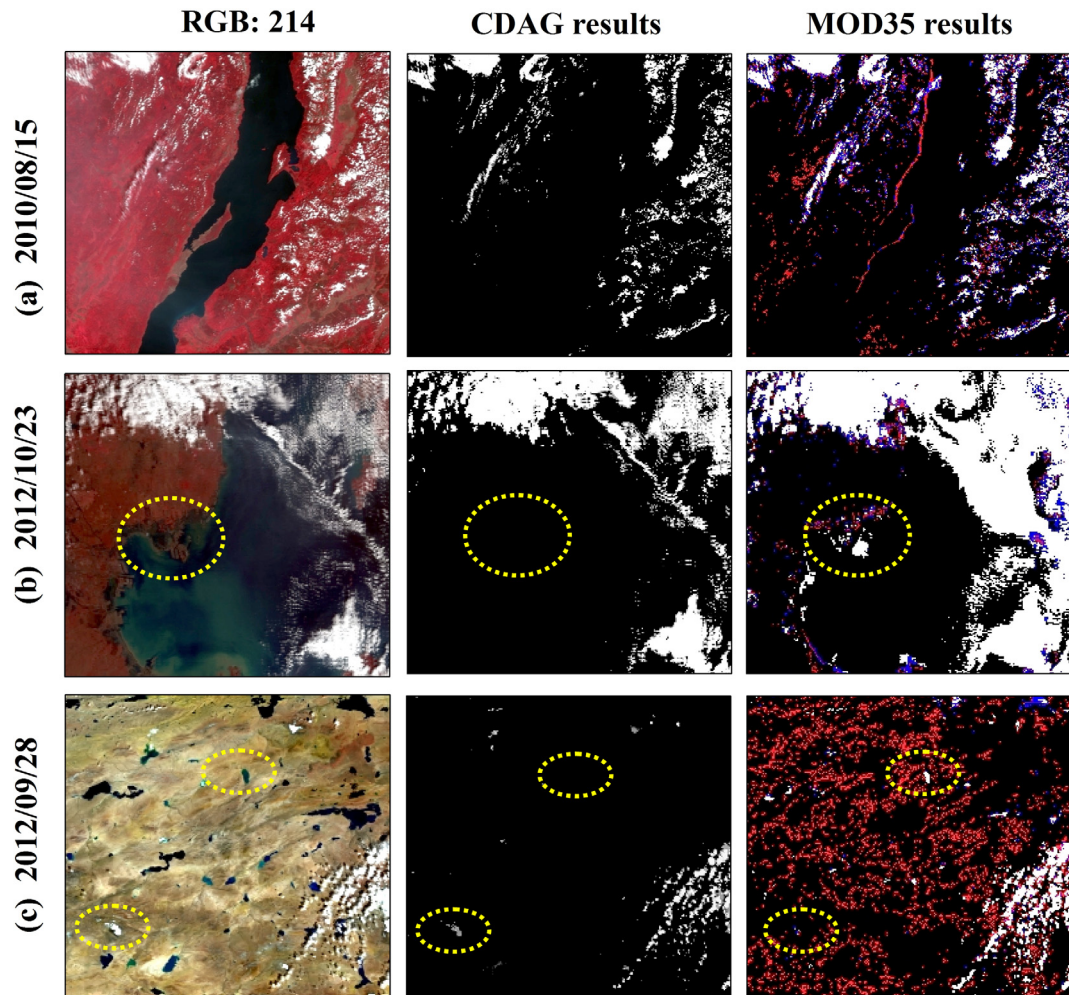


Fig. 14. Comparison of the MODIS cloud detection results with the quasi-synchronous MODIS cloud detection products (MOD35). A: Result of Lake Baikal acquired at 0400 UTC time on August 15, 2010. B: Result of the Bohai Sea coastal area acquired at 0320 UTC time on October 22, 2012. C: Result of Tibet, China, acquired at 0505 UTC time on September 27, 2012. In each scene, the left shows a false color composited MODIS image with bands 2, 1 and 4 as red, green and blue, respectively, and in the middle of the cloud test results, the right shows the MOD35 result in which white represents clouds, red represents uncertain clear sky, blue is probable clear sky, and black is confident clear sky. (For interpretation of the references to color in this figure legend, the reader is referred to the web version of this article.)

Table 7
Quantitative analysis of CDAG cloud detection results with three different detection images, including Landsat8 OLI, MODIS, and NPP VIIRS data corresponding to Figs. 10, 11, and 12, respectively.

Data	Image number	Cloudy pixels correct rate	Clear sky pixels correct rate	Error rate	Missing rate
Landsat 8 OLI	A	0.932	0.981	0.019	0.068
	B	0.978	0.997	0.003	0.022
	C	0.952	0.980	0.020	0.048
	D	0.906	0.978	0.022	0.094
	E	0.874	0.895	0.105	0.126
	F	0.915	0.897	0.103	0.085
NPP VIIRS	A	0.932	0.902	0.068	0.098
	B	0.894	0.957	0.106	0.043
	C	0.922	0.960	0.078	0.040
	D	0.902	0.889	0.098	0.111
	E	0.946	0.898	0.054	0.102
	F	0.925	0.875	0.074	0.125
MODIS	A	0.911	0.947	0.053	0.089
	B	0.939	0.964	0.036	0.061
	C	0.917	0.941	0.059	0.083
	D	0.893	0.967	0.033	0.107
	E	0.974	0.905	0.095	0.026
	F	0.933	0.899	0.101	0.067
	G	0.982	0.998	0.002	0.018
	H	0.884	0.999	0.001	0.116

$$\text{Cloud pixels correct rate} = \frac{\text{TP}}{\text{Cloud pixels in reference data}} \quad (7)$$

$$\text{Clear sky pixels correct rate} = \frac{\text{TN}}{\text{Clear sky pixels in reference data}} \quad (8)$$

$$\text{Error rate} = \frac{\text{FP}}{\text{Clear sky pixels in reference data}} \quad (9)$$

$$\text{Missing rate} = \frac{\text{FN}}{\text{Cloud pixels in reference data}} \quad (10)$$

where the true positive (TP) represents both the reference data and the detection method classify the pixel as a cloud; true negative (TN) represents both the reference data and the detection method classify the pixel as clear sky; False positive (FP) represents the reference data classifies the pixel as clear sky, but the detection method classifies the pixel as a cloud; False negative (FN) represents the reference data classifies the pixel as a cloud, but the detection method classifies the pixel as clear sky.

Table 7 presents the quantitative evaluation results for the Landsat 8 OLI, NPP VIIRS, and MODIS data. The image number of

the three types of data in the table corresponds to the images in Figs. 10, 11, and 12, respectively. The accuracy evaluation matrix shows that this method has good measurement precision for the three types of data, with an overall precision of 0.85, and a lower degree of misjudgment of clear skies. The type and amount of cloud can also influence the overall precision. Images with a higher amount of thick clouds have greater precision, and those with few clouds have lower precision. The accuracy of images with a greater amount of thick clouds and broken clouds is relatively stable with relatively high precision compared to the image with more thin clouds. Less misjudgment and small fluctuations in the error rate and missing rate meet the requirements for daily use. Various surface types in images can also affect the precision. Images with large urban areas have higher misjudgment rates than those with farmlands or forests. The above experiments and studies clearly demonstrate that the algorithm proposed in this paper is comprehensive and can yield reliable cloud detection results when applied to Landsat 8 OLI, Terra MODIS, and NPP VIIRS data.

6. Summary and conclusions

This paper presents a CDAG method for cloud detection from multi-sensor remote sensing data, and the detection results were associated with the accuracy of the algorithms. The CDAG method is based on high spatial resolution, and the hyperspectral remote sensing data automatically generates the cloud detection algorithm through data simulation, band tests, statistical analysis, algorithm sorting, etc. Different tests are used for the synthesis of cloud probability results according to the accuracy and threshold. The results were verified by a plurality of Landsat 8 OLI, Terra MODIS and Suomi NPP VIIRS images and by a comparison with Fmask cloud product and quasi-synchronous MODIS cloud products (MOD35), which yielded good results. A statistical comparison with the vectorization results yielded an overall precision of selected images of greater than 85%. In general, the CDAG method can effectively reduce the cloud effect; identify thick, thin and broken clouds over different surface types; and remove the effects of various surface types, such as vegetation, water, snow and desert. The detection precision could be further improved by different detection tests, making it efficient, accurate and suitable for business-oriented applications.

Automating cloud detection for multi-sensor data is difficult because clouds have similar spectral information to some surfaces. The CDAG method makes use of the spectral information in visible to SWIR wavelengths to generate cloud detection results based on the spectral differences between cloudy and clear-sky pixels. Additionally, the threshold of the CDAG method is automatically determined based on the error rate of the pixel dataset, which reduces the impact of human factors. Moreover, the different cloud detection algorithms must be evaluated for different sensor data, which is time-consuming and not conducive to the expansion of future work. The method proposed in this paper is applicable to various sensor data and requires only a SRF of the detected multispectral data. In addition, the CDAG method can process a large amount of remote sensing data in batches with simple operation, high efficiency, a fast running speed and a high degree of automation.

Acknowledgments

The authors thank the National Natural Science Foundation of China [41171270] and the Outstanding Youth Fund of Shandong Province [JQ201211]. The AVIRIS, Landsat 8 OLI, MODIS Terra, and Suomi NPP VIIRS data are available from the National Aeronautics and Space Administration (NASA) websites. The authors also

thank Z. Zhu and C.E. Woodcock for providing the codes for the Fmask algorithm.

References

- Ackerman, S., Strabala, K., Menzel, P., Frey, R., Moeller, C., Gumley, L., 2010. Discriminating Clear-Sky from Cloud with MODIS Algorithm Theoretical Basis Document (MOD35). MODIS Cloud Mask Team, Cooperative Institute for Meteorological Satellite Studies, University of Wisconsin.
- Ackerman, S.A., Strabala, K.I., Menzel, W.P., 1998. Discriminating clear sky from clouds with MODIS. *J. Geophys. Res.* 103 (D24), 32141–32157.
- Baugh, W.M., Kruse, F.A., Atkinson, W.W., 1998. Quantitative geochemical mapping of ammonium minerals in the southern cedar mountains, Nevada, using the airborne visible/infrared imaging spectrometer (AVIRIS). *Rem. Sens. Environ.* 65 (3), 292–308.
- Blonski, S., Glasser, G., Russell, J., Ryan, R., Terrie, G., Zanoni, V., 2003. Synthesis of multispectral bands from hyperspectral data: validation based on images acquired by AVIRIS, HYPERION, ALI, and ETM+. In: 2002 AVIRIS Earth Science and Applications Workshop, Pasadena, CA; United States, 5–8 March.
- Carslaw, K.S., Harrison, R.G., Kirkby, J., 2002. Cosmic rays, clouds, and climate. *Science* 298 (5599), 1732–1737.
- Chang, F., Li, Z., 2005. A new method for detection of cirrus overlapping water clouds and determination of their optical properties. *J. Atmos. Sci.* 62 (11), 3993–4009.
- Frey, R.A., Ackerman, S.A., Liu, Y., 2008. Cloud detection with MODIS. Part I: improvements in the MODIS cloud mask for collection 5. *J. Atmos. Oceanic Technol.* 25 (7), 1057–1072.
- Gao, B., Goetz, A.F.H., Wiscombe, W.J., 1993. Cirrus cloud detection from airborne imaging spectrometer data using the 1.38 μm water vapor band. *Geophys. Res. Lett.* 20 (4), 301–304.
- Gesell, G., 1989. An algorithm for snow and ice detection using AVHRR data an extension to the APOLLO software package. *Int. J. Rem. Sens.* 10 (4–5), 897–905.
- Goodwin, N.R., Collett, L.J., Denham, R.J., Flood, N., Tindall, D., 2013. Cloud and cloud shadow screening across Queensland, Australia: an automated method for Landsat TM/ETM+ time series. *Rem. Sens. Environ.* 134, 50–65.
- Green, R.O., Eastwood, M.L., Sarture, C.M., Chrien, T.G., Aronsson, M., Chippendale, B. J., Faust, J.A., Pavri, B.E., Chovit, C.J., Solis, M., Olah, M.R., Williams, O., 1998. Imaging spectroscopy and the airborne visible/infrared imaging spectrometer (AVIRIS). *Rem. Sens. Environ.* 65 (3), 227–248.
- Green, R.O., Shimada, M., 1997. On-orbit calibration of a multi-spectral satellite sensor using a high altitude airborne imaging spectrometer. *Adv. Space Res.* 19 (9), 1387–1398.
- Greenhough, J., Remedios, J.J., Sembhi, H., Kramer, L.J., 2005. Towards cloud detection and cloud frequency distributions from MIPAS infra-red observations. *Adv. Space Res.* 36 (5), 800–806.
- Guo, Y., Li, L., Jin, L., et al., 2013. Study on cloud processing methods with MODIS data. In: 2013 IEEE 5th International Symposium on Microwave, Antenna, Propagation and EMC Technologies for Wireless Communications (MAPE), IEEE, Chengdu, China, 29–31 October, pp. 694–696.
- Hagolle, O., Huc, M., Pascual, D.V., Dedieu, G., 2010. A multi-temporal method for cloud detection, applied to FORMOSAT-2, VENµS, LANDSAT and SENTINEL-2 images. *Rem. Sens. Environ.* 114 (8), 1747–1755.
- Harshvardhan, Randall, D.A., Corsetti, T.G., 1989. Earth radiation budget and cloudiness simulations with a general circulation model. *J. Atmos. Sci.* 46 (13), 1922–1942.
- Hégarat-Mascle, S.L., André, C., 2009. Use of markov random fields for automatic cloud/shadow detection on high resolution optical images. *ISPRS J. Photogramm. Rem. Sens.* 64 (4), 351–366.
- Hillger, D., Seaman, C., Liang, C., Miller, S., Lindsey, D., Kopp, T., 2014. Suomi NPP VIIRS imagery evaluation. *J. Geophys. Res.: Atmos.* 119 (11), 6440–6455.
- Hutchison, K.D., Isager, B.D., Mahoney, R.L., 2013. Enhanced snow and ice identification with the VIIRS cloud mask algorithm. *Rem. Sens. Lett.* 4 (9), 929–936.
- Irish, R.R., Barker, J.L., Goward, S.N., Arvidson, T., 2006. Characterization of the landsat-7 ETM+ automated cloud-cover assessment (ACCA) algorithm. *Photogramm. Eng. Rem. Sens.* 72 (10), 1179–1188.
- Jedlovec, G.J., Haines, S.L., LaFontaine, F.J., 2008. Spatial and temporal varying thresholds for cloud detection in GOES imagery. *IEEE Trans. Geosci. Rem. Sens.* 46 (6), 1705–1717.
- Kazantzidis, A., Eleftheratos, K., Zerefos, C.S., 2011. Effects of cirrus cloudiness on solar irradiance in four spectral bands. *Atmos. Res.* 102 (4), 452–459.
- Kazantzidis, A., Tzoumanikas, P., Bais, A.F., Fotopoulos, S., Economou, G., 2012. Cloud detection and classification with the use of whole-sky ground-based images. *Atmos. Res.* 113, 80–88.
- King, M.D., Platnick, S., Menzel, W.P., Ackerman, S.A., Hubanks, P.A., 2013. Spatial and temporal distribution of clouds observed by MODIS onboard the Terra and aqua satellites. *IEEE Trans. Geosci. Rem. Sens.* 51 (7), 3826–3852.
- Kopp, T.J., Thomas, W., Heidinger, A.K., Botambekov, D., Frey, R.A., Hutchison, K.D., Isager, B.D., Brueske, K., Reed, B., 2014. The VIIRS cloud mask: progress in the first year of S-NPP toward a common cloud detection scheme. *J. Geophys. Res.: Atmos.* 119 (5), 2441–2456.
- Kriebel, K.T., Saunders, R.W., Gesell, G., 1989. Optical properties of clouds derived from fully cloudy AVHRR pixels. *Beiträge zur Physik der Atmosphäre* 62, 165–171.

- Kriebel, K.T., Gesell, G., Kästner, M., Mannstein, H., 2003. The cloud analysis tool APOLLO: improvements and validations. *Int. J. Rem. Sens.* 24 (12), 2389–2408.
- Li, H., Zhang, L., Shen, H., Li, P., 2012. A variational gradient-based fusion method for visible and SWIR imagery. *Photogramm. Eng. Rem. Sens.* 78 (9), 947–958.
- Li, Q., Lu, W., Yang, J., 2011. A hybrid thresholding algorithm for cloud detection on ground-based color images. *J. Atmos. Oceanic Technol.* 28 (10), 1286–1296.
- Li, Z., Shen, H., Li, H., Xia, G., Gamba, P., Zhang, L., 2016. Multi-feature combined cloud and cloud shadow detection in GF-1 WFV imagery. arXiv preprint arXiv: 1606.05415.
- Lin, C., Lin, B., Lee, K., Chen, Y., 2015. Radiometric normalization and cloud detection of optical satellite images using invariant pixels. *ISPRS J. Photogramm. Rem. Sens.* 106, 107–117.
- Maierperger, T.K., Scaramuzza, P.L., Leigh, L., Shrestha, S., Gallo, K.P., Jenkerson, C.B., Dwyer, J.L., 2013. Characterizing LEDAPS surface reflectance products by comparisons with AERONET, field spectrometer, and MODIS data. *Rem. Sens. Environ.* 136, 1–13.
- Murino, L., Amato, U., Carfora, M.F., Antoniadis, A., Huang, B., Menzel, W.P., Serio, C., 2014. Cloud detection of MODIS multispectral images. *J. Atmos. Oceanic Technol.* 31 (2), 347–365.
- Nakajima, T.Y., Tsuchiya, T., Ishida, H., Matsui, T.N., Shimoda, H., 2011. Cloud detection performance of spaceborne visible-to-infrared multispectral imagers. *Appl. Opt.* 50 (17), 2601–2616.
- Rossow, W.B., Garder, L.C., 1993. Cloud detection using satellite measurements of infrared and visible radiances for ISCCP. *J. Clim.* 6 (12), 2341–2369.
- Rossow, W.B., Mosher, F., Kinsella, E., 1985. ISCCP cloud algorithm intercomparison. *J. Clim. Appl. Meteorol.* 24 (9), 877–903.
- Rossow, W.B., Schiffer, R.A., 1991. ISCCP cloud data products. *Bull. Am. Meteorol. Soc.* 72 (1), 2–20.
- Roy, D.P., Wulder, M.A., Loveland, T.R., Woodcock, C.E., Allen, R.G., Anderson, M.C., Helder, D., Irons, J.R., Johnson, D.M., Kennedy, R., Scambos, T.A., Schaaf, C.B., Schott, J.R., Sheng, Y., Vermote, E.F., Belward, A.S., Bindschadler, R., Cohen, W.B., Gao, F., Hippel, J.D., 2014. Landsat-8: science and product vision for terrestrial global change research. *Rem. Sens. Environ.* 145, 154–172.
- Saunders, R.W., Kriebel, K.T., 1988. An improved method for detecting clear sky and cloudy radiances from AVHRR data. *Int. J. Rem. Sens.* 9 (1), 123–150.
- Sedano, F., Kempeneers, P., Strobl, P., Kucera, J., Vogt, P., Seebach, L., et al., 2011. A cloud mask methodology for high resolution remote sensing data combining information from high and medium resolution optical sensors. *ISPRS J. Photogramm. Rem. Sens.* 66 (5), 588–596.
- Shi, T., Yu, B., Clothiaux, E.E., Braverman, A.J., 2008. Daytime Arctic cloud detection based on multi-angle satellite data with case studies. *J. Am. Stat. Assoc.* 103 (482), 584–593.
- Stowe, L.L., McClain, E.P., Carey, R., 1991. Global distribution of cloud cover derived from NOAA/AVHRR operational satellite data. *Adv. Space Res.* 11 (3), 51–54.
- Sun, L., Sun, C., Liu, Q., Zhong, B., 2010. Aerosol optical depth retrieval by HJ-1/CCD supported by MODIS surface reflectance data. *Sci. China Earth Sci.* 53 (S1), 74–80.
- Sun, L., Wei, J., Bilal, M., Tian, X., Jia, C., Guo, Y., Mi, X., 2015. Aerosol optical depth retrieval over Bright areas using landsat 8 OLI images. *Rem. Sens.* 8 (1), 23.
- Sun, L., Wei, J., Wang, J., Mi, X., Guo, Y., Lv, Y., et al., 2016. A universal dynamic threshold cloud detection algorithm (UDTCDA) supported by a prior surface reflectance database. *J. Geophys. Res. Atmos.* 121 (12), 7172–7196.
- Van der Meer, F., 1994. Calibration of airborne visible/infrared imaging spectrometer data (AVIRIS) to reflectance and mineral mapping in hydrothermal alteration zones: an example from the “cuprite mining district”. *Geocarto Int.* 9 (3), 23–37.
- Vane, G., Green, R.O., Chrien, T.G., Enmark, H.T., Hansen, E.G., Porter, W.M., 1993. The airborne visible/infrared imaging spectrometer (AVIRIS). *Rem. Sens. Environ.* 44 (2–3), 127–143.
- Yang, J., Lu, W., Ma, Y., Yao, W., 2012. An automated cirrus cloud detection method for a ground-based cloud image. *J. Atmos. Oceanic Technol.* 29 (4), 527–537.
- Yang, Y., Marshak, A., Palm, S.P., Wang, Z., Schaaf, C., 2013. Assessment of cloud screening with apparent surface reflectance in support of the icesat-2 mission. *IEEE Trans. Geosci. Rem. Sens.* 51 (2), 1037–1045.
- Wei, J., Ming, Y.F., Han, L.S., Ren, Z.L., Guo, Y.M., 2015. Method of remote sensing identification for mineral types based on multiple spectral characteristic parameters matching. *Spectrosc. Spectr. Anal.* 35, 2862–2866.
- Zanoni, V., Davis, B., Ryan, R., Gasser, G., Blonski, S., 2002. Remote sensing requirements development: a simulation-based approach. In: Proc. ISPRS Commission I Mid-Term, Symposium 2002: Integrated Remote Sensing at the Global, Regional and Local Scale, Denver, CO, 8–15 November, pp. 10–15.
- Zhang, Y., Guindon, B., 2003. Quantitative assessment of a haze suppression methodology for satellite imagery: effect on land cover classification performance. *IEEE Trans. Geosci. Rem. Sens.* 41 (5), 1082–1089.
- Zhang, Y., Guindon, B., Cihlar, J., 2002. An image transform to characterize and compensate for spatial variations in thin cloud contamination of landsat images. *Rem. Sens. Environ.* 82 (2–3), 173–187.
- Zhu, Z., Wang, S., Woodcock, C.E., 2015. Improvement and expansion of the Fmask algorithm: cloud, cloud shadow, and snow detection for Landsats, pp. 4–7, 8, and Sentinel 2 images. *Rem. Sens. Environ.* 159, 269–277.
- Zhu, Z., Woodcock, C.E., 2012. Object-based cloud and cloud shadow detection in landsat imagery. *Rem. Sens. Environ.* 118, 83–94.
- Zhu, Z., Woodcock, C.E., 2014. Automated cloud, cloud shadow, and snow detection in multitemporal landsat data: an algorithm designed specifically for monitoring land cover change. *Rem. Sens. Environ.* 152, 217–234.